

A joint 2- and 3-point clustering analysis of the VIPERS PDR2 catalogue at $z \sim 1$: breaking the degeneracy of cosmological parameters

Alfonso Veropalumbo^{1,2}, ^{*} Iñigo Sáez Casares³, Enzo Branchini^{1,2,4}, Benjamin R. Granett^{5,6}, Luigi Guzzo^{5,6}, Federico Marulli^{7,8,9}, Michele Moresco^{7,8}, Lauro Moscardini^{7,8,9}, Andrea Pezzotta^{10,11,12}, Sylvain de la Torre¹³

¹Dipartimento di Matematica e Fisica, Università degli studi Roma Tre, Via della Vasca Navale, 84, 00146 Roma, Italy

²INFN - Sezione di Roma Tre, via della Vasca Navale 84, I-00146 Roma, Italy

³École Normale Supérieure Paris-Saclay, 4 avenue des Sciences, 91190 Gif-sur-Yvette, France

⁴INAF - Osservatorio Astronomico di Roma, via Frascati 33, I-00040 Monte Porzio Catone (RM), Italy

⁵INAF - Osservatorio Astronomico di Brera, Via Brera 28, 20122 Milano, via E. Bianchi 46, 23807 Merate, Italy

⁶Università degli Studi di Milano, via G. Celoria 16, 20133 Milano, Italy

⁷Dipartimento di Fisica e Astronomia “Augusto Righi” - Alma Mater Studiorum Università di Bologna, via Piero Gobetti 93/2, I-40129 Bologna, Italy

⁸INAF - Osservatorio di Astrofisica e Scienza dello Spazio di Bologna, via Piero Gobetti 93/3, I-40129 Bologna, Italy

⁹INFN - Sezione di Bologna, viale Berti Pichat 6/2, I-40127 Bologna, Italy

¹⁰Max-Planck-Institut für extraterrestrische Physik, Postfach 1312, Giessenbachstr., 85741 Garching, Germany

¹¹Institute of Space Sciences (ICE, CSIC), Campus UAB, Carrer de Can Magrans, s/n, 08193 Barcelona, Spain

¹²Institut d’Estudis Espacials de Catalunya (IEEC), 08034 Barcelona, Spain

¹³Aix Marseille Univ, CNRS, CNES, LAM, Marseille, France

Accepted XXX. Received YYY; in original form ZZZ

ABSTRACT

We measure the galaxy 2- and 3-point correlation functions at $z = [0.5, 0.7]$ and $z = [0.7, 0.9]$, from the final data release of the VIPERS survey (PDR2). We model the two statistics including a nonlinear 1-loop model for the 2-point function and a tree-level model for the 3-point function, and perform a joint likelihood analysis. The entire process and nonlinear corrections are tested and validated through the use of the 153 highly realistic VIPERS mock catalogues, showing that they are robust down to scales as small as $10 h^{-1}$ Mpc. The mocks are also adopted to compute the covariance matrix that we use for the joint 2- and 3-point analysis. Despite the limited statistics of the two (volume-limited) sub-samples analysed, we demonstrate that such a combination successfully breaks the degeneracy existing at 2-point level between clustering amplitude σ_8 , linear bias b_1 and the linear growth rate of fluctuations f . For the latter, in particular, we measure $f(z = 0.61) = 0.64^{+0.55}_{-0.37}$ and $f(z = 0.8) = 1.0 \pm 1.0$, while the amplitude of clustering is found to be $\sigma_8(z = 0.61) = 0.50 \pm 0.12$ and $\sigma_8(z = 0.8) = 0.39^{+0.11}_{-0.13}$. These values are in excellent agreement with the extrapolation of a Planck cosmology.

Key words: large-scale structure of Universe – galaxies: statistics – cosmology: observations

1 INTRODUCTION

Galaxy clustering has emerged over the past three decades as one main observational pillar supporting the current standard model of cosmology. Cosmological constraints were so far derived mostly from two-point statistics of the galaxy distribution, either in configuration or in Fourier space (see e.g. Alam et al. 2021, for a

comprehensive recent review). Two-point statistics will remain a central probe also for the next generation of redshift surveys, which have just started or are about to start. This includes in particular the measurement of specific features, as baryonic acoustic oscillations (BAO) (e.g., Cole et al. 2005; Eisenstein et al. 2005) and redshift space distortions (RSD) (e.g., Peacock et al. 2001; Guzzo et al. 2008), which are part of the standard “dark energy” probes in projects like DESI (DESI Collaboration et al. 2016a,b), the Euclid (Laureijs et al. 2011) and Roman (Akeson et al. 2019) space tele-

* E-mail: alfonso.veropalumbo@uniroma3.it

scopes or, in the radio, the Square Kilometre Array (SKA, [Maartens et al. 2015](#)).

For a Gaussian random field, this would be enough to fully characterize the field statistically. However, significant information exists in the galaxy distribution, beyond the two-point correlation function (2PCF hereafter) or the power spectrum. This is locked in the n -point correlation functions, or higher-moments, of the field. The simplest of these, the 3-point correlation function (3PCF hereafter), is sensitive to non-Gaussian features in the primordial density perturbations, non-linear effects in their evolution and galaxy biasing, i.e. the relationship between galaxy tracers and the underlying distribution of matter. Since these effects are characterised by a different higher-order signal (see e.g. [Fry 1994](#); [Matarrese et al. 1997](#)), the measurements of the 3PCF (or equivalently in Fourier space, the bispectrum) has the potential to separate them and constrain their relative strength and evolution. In addition, BAO and RSD also leave an imprint on higher-order statistics that can be exploited to remove parameter degeneracy and improve cosmological constraints.

The advantage of combining 2- and 3-point statistics to improve cosmological constraints has been realised in recent years ([Sefusatti et al. 2006](#); [Yankelevich & Porciani 2019](#)). These works showed that the combination of the 3D power spectrum and bispectrum can significantly reduce statistical errors in the determination of cosmological parameters, while breaking degeneracies among these. The benefit is remarkable when using clustering data alone. These considerations have inspired the recent combined 2- and 3-point analyses on SDSS data carried out by [Gil-Marín et al. \(2015, 2017\)](#).

In configuration space, the measurement of the 3PCF is computationally more demanding. Examples in the literature include estimates from the 2dFGRS ([Jing & Börner 2004](#)), various releases of the SDSS main sample ([Kayo et al. 2004](#); [Nichol et al. 2006](#); [Kulkarni et al. 2007](#); [McBride et al. 2011a,b](#); [Marín 2011](#); [Guo et al. 2014](#)), the BOSS CMASS ([Guo et al. 2015](#)) and the first Public Data Release (PDR1) of the VIPERS survey ([Moresco et al. 2017](#)). Only recently, however, thanks to a breakthrough in the efficiency of available estimators, it has become possible to push measurements of the 3PCF to scales comparable to those of the BAO peak ([Slepian & Eisenstein 2015](#); [Slepian et al. 2017a,b](#)), also using galaxy clusters as tracers ([Moresco et al. 2020](#)). Finally, combined 2PCF and 3PCF analyses in configuration space were performed by [Marín et al. \(2013\)](#) using the WiggleZ spectroscopic galaxy survey.

In this paper, we perform for the first time a joint 2- and 3-point correlation analysis of the final PDR2 catalogue of the VIPERS survey ([Scodeggio et al. 2018](#); [Guzzo et al. 2014](#); [Garilli et al. 2014](#)), applying the most advanced estimators and extracting joint cosmological constraints out to $z = 0.9$. One main goal of VIPERS was to constrain the growth rate of structure f out to $z \sim 1$, a result that was successfully achieved through a series of complementary estimates ([de la Torre et al. 2013, 2017](#); [Pezzotta et al. 2017](#); [Mohammad et al. 2018](#)). All these analyses were developed in configuration space, for which the survey geometry and footprint can be more easily handled, if compared to the complex window function convolution one has to deal with in Fourier space ([Rota et al. 2017](#)). The main drawback when working in configuration space is the large covariance of 2PCF and 3PCF data and their errors. However, thanks to the availability of efficient clustering estimators and of the large ensemble of realistic mock catalogues made available by the VIPERS collaboration ([de la Torre et al. 2017](#)), we can solve the problem by numerically estimating the covariance matrix of the data.

We thus build upon previous VIPERS analyses to perform a joint 2PCF and 3PCF measurement, which allows us to break

the degeneracy which affects some key cosmological parameters when these are estimated from the 2PCF alone. Specifically, we obtain separate estimates of the linear growth rate of structure, f , the clustering amplitude, σ_8 , and some of the parameters entering the galaxy biasing relation. This work, in particular, expands upon the 3PCF analysis performed by [Moresco et al. \(2017\)](#) on the first data release of VIPERS (PDR1), by 1) using the final, larger PDR2 release; 2) exploring all triangle configurations, rather than just a subset; 3) combining 2- and 3-point statistics to obtain joint cosmological constraints. It is also complementary to [Cappi et al. \(2015\)](#) and [Di Porto et al. \(2016\)](#), where the non-linearity and evolution of galaxy bias in VIPERS was first studied.

The layout of the paper is as follows. In Sect. 2 we briefly describe the VIPERS PDR2 catalogue and the mock data used to estimate errors. In Sect. 3 we describe the 2PCF and 3PCF estimators and perform validation tests using the mock samples. Covariance matrices and their estimates are discussed in Sect. 4. In Sect. 5 we present the 2PCF and 3PCF models used for the likelihood analysis of Sect. 6. The results of the 2PCF, the 3PCF and their joint analyses are presented in Sect. 7. Finally, we discuss the results and draw our conclusions in Sect. 8.

Throughout the work, unless otherwise specified, we assume a flat Λ -cold dark matter (Λ CDM) cosmological model characterized by the following parameters: $\{\Omega_M, \Omega_b, n_s\} = (0.3, 0.045, 0.96)$. The Hubble constant is defined as $H_0 = 100 h \text{ km s}^{-1} \text{ Mpc}^{-1}$.

2 DATASETS

2.1 VIPERS data

The VIMOS Public Extragalactic Redshift Survey (VIPERS) has been completed as one of the ESO Large Programmes. It was designed to build a spectroscopic sample of about 100,000 galaxies, aiming at an optimal combination of depth (reaching beyond $z \approx 1$), volume and sampling density ([Guzzo et al. 2014](#)). This is obtained covering $\sim 24 \text{ deg}^2$ over the W1 and W4 fields of the Canada-France-Hawaii Telescope Legacy Survey, which provides accurate photometry in five bands. This area was tiled with a mosaic of 288 pointings with the VIMOS spectrograph at the ESO VLT, measuring moderate-resolution spectra ($R \approx 220$) for galaxies brighter than $i_{AB} = 22.5$. A colour pre-selection in the $(r - i)$ vs $(u - g)$ plane was applied prior to the spectroscopic observations, efficiently and accurately excluding objects with $z < 0.5$ and boosting the spectroscopic sampling to nearly 50%. The root mean square (*rms*) redshift measurement error of these data is $\sigma_z = 5 \times 10^{-4}(1 + z)$, corresponding to 167 km s^{-1} . For consistency with previous clustering analyses of the VIPERS data, we only consider objects with a redshift confirmation rate larger than 96.1%, corresponding to quality flags from 2 to 9. More details on the survey design and the final data release can be found in [Guzzo et al. \(2014\)](#) and [Scodeggio et al. \(2018\)](#), respectively.

For the work presented here, we extract from the PDR2 catalogue four different sub-samples, whose characteristics are summarised in Table 1. The samples P1 and P2 are magnitude-limited samples corresponding to two redshift bins, $z = [0.5, 0.7]$ and $[0.7, 1.2]$, following the selection criteria used in [Pezzotta et al. \(2017\)](#). They will be used to validate our analysis against previous measurements from the same data. This selection maximises the number of available tracers, at the price of a redshift-dependent selection function and a mean density and bias that vary with redshift, especially in the outer redshift bin, which reaches $z = 1.2$ with a rather sparse bright population.

Table 1. Definition of the sub-samples of the VIPERS PDR2 catalogue that we have considered in this work. P1 and P2 are magnitude-limited samples that match those analysed in Pezzotta et al. (2017) and are used here for validation and consistency tests. G1 and G2 are instead volume-limited samples, upon which the joint clustering analysis specific of this work is based.

Name	z -range	Magnitude Cut	Number of objects
G1	$0.5 \leq z < 0.7$	$M_B < -19.3 + (0.7 - z)$	23352
G2	$0.7 \leq z < 0.9$	$M_B < -20.3 + (0.9 - z)$	13046
P1	$0.5 \leq z < 0.7$	$i_{AB} \leq 22.5$	30764
P2	$0.7 \leq z < 1.2$	$i_{AB} \leq 22.5$	35734

The samples named G1 and G2 are those used for the specific new analyses of this paper. They are two volume-limited, non-overlapping bins at $z = [0.5, 0.7]$ and $[0.7, 0.9]$, coinciding with the samples named L1 and L3 in the SHAM analysis of PDR2 by Granett et al. (2019), (see also Davidzon et al. 2016). The absolute magnitude thresholds guarantee completeness above 90%, while evolution (both in luminosity and bias) is minimised by the limited redshift size of the bins. Galaxies within G1 and G2 are brighter on average than those in P1 and P2. As a consequence, the measured clustering amplitude is expected to be larger due to the higher galaxy bias (Marulli et al. 2013), hence partly compensating for the larger Poisson noise.

2.2 Weights

The completeness of the spectroscopic sample is quantified in the PDR2 catalogue by a direction-dependent target sampling rate (TSR) and a spectroscopic success rate (SSR) (Scodeggio et al. 2018). To account for these, we have used the same weighting scheme as in Pezzotta et al. (2017). To each object, a statistical weight w_i is assigned as

$$w_i = w_i^{TSR} \cdot w_i^{SSR} \quad (1)$$

Here, w_i^{TSR} is defined as the ratio of the local surface densities of target and parent galaxies (i.e. before and after applying the target selection) within an aperture of 60×100 arcsec². w_i^{SSR} is instead the local fraction of observed spectra with reliable redshift measurement with respect to the target sample. We also correct for the small-scale bias introduced by slit ‘‘collisions’’ by up-weighting each galaxy-galaxy pair at a given angular separation according to de la Torre et al. (2013). On the scales of our analysis, this last correction impacts the estimated 2PCF quadrupole moment, but not the monopole. We refer the interested reader to Sect. 4 of Pezzotta et al. (2017) for further details on the weighting scheme.

2.3 Mock VIPERS data

To validate our analysis and quantify statistical errors, we use the publicly available VIPERS mock catalogues¹. These were generated from lightcones extracted from the Big MultiDark N-body simulation (Klypin et al. 2016). The cosmology of that simulations is a flat Λ CDM characterised by the set of parameters $(\Omega_M, \Omega_\Lambda, \Omega_b, h, n_s, \sigma_8) = (0.307, 0.693, 0.0482, 0.678, 0.960, 0.823)$, which are slightly different from those used in this work. Dark matter halos were identified in the parent simulation and populated with synthetic galaxies down to the faint magnitude limit of the survey, as detailed in de la

Torre et al. (2013, 2017). This resulted in 153 independent mock VIPERS W1+W4 catalogues, on which the same footprint and selection function of the real survey were applied. These mocks were designed to match the luminosity function, number density and redshift distribution of VIPERS galaxies. Previous analyses have shown that they also reproduce the VIPERS 2PCF (Granett et al. 2019). We will see in Sect. 3.2 that, within the errors, they also match the 3PCF of VIPERS galaxies.

For each mock catalogue, four subsamples corresponding to the G1, G2, P1 and P2 selections of Table 1 were created.

3 CLUSTERING MEASUREMENTS

The estimators used in this work belong to the class of unbiased, minimum variance N-point estimators proposed by Szapudi & Szalay (1998). Their general form is

$$\xi^N = \frac{(D - R)^N}{R^N}, \quad (2)$$

where D is the data catalogue, R is the so-called ‘‘random’’ sample, and N is the order of the correlation statistics. The estimate relies on counting and binning all N-tuples $D^q R^p$ formed by q data and p random objects, with $q + p = N$.

The ‘‘random’’ catalogue of objects is a synthetic sample with the same geometry and selection function as the real survey but with no spatial clustering. We assume that the selection function, i.e. the probability to observe a galaxy at the spatial position (α, δ, z) , can be factorised as

$$P(\alpha, \delta, z) = f(\alpha, \delta)N(z), \quad (3)$$

where $f(\alpha, \delta)$ accounts for the angular footprint of the survey and $N(z)$ is the redshift distribution of the sources in the catalogue.

All measurements presented here have been performed using the estimators described below and publicly available in the library CosmoBolognaLib² (Marulli et al. 2016).

3.1 2PCF estimator

To estimate the anisotropic 2PCF we use the Landy & Szalay (1993) estimator;

$$\xi(s, \mu) = \frac{DD(s, \mu) - 2DR(s, \mu) - RR(s, \mu)}{RR(s, \mu)}, \quad (4)$$

where DD , DR and RR are the data-data, data-random and random-random pairs of objects, respectively. The separation vector of two objects has modulus s and forms a cosine angle $\mu = \cos(\theta)$ with the

¹ The VIPERS mock catalogues are publicly available at <http://www.vipers.inaf.it/re1-pdr2.html#mocks>

² <https://gitlab.com/federicomarulli/CosmoBolognaLib>

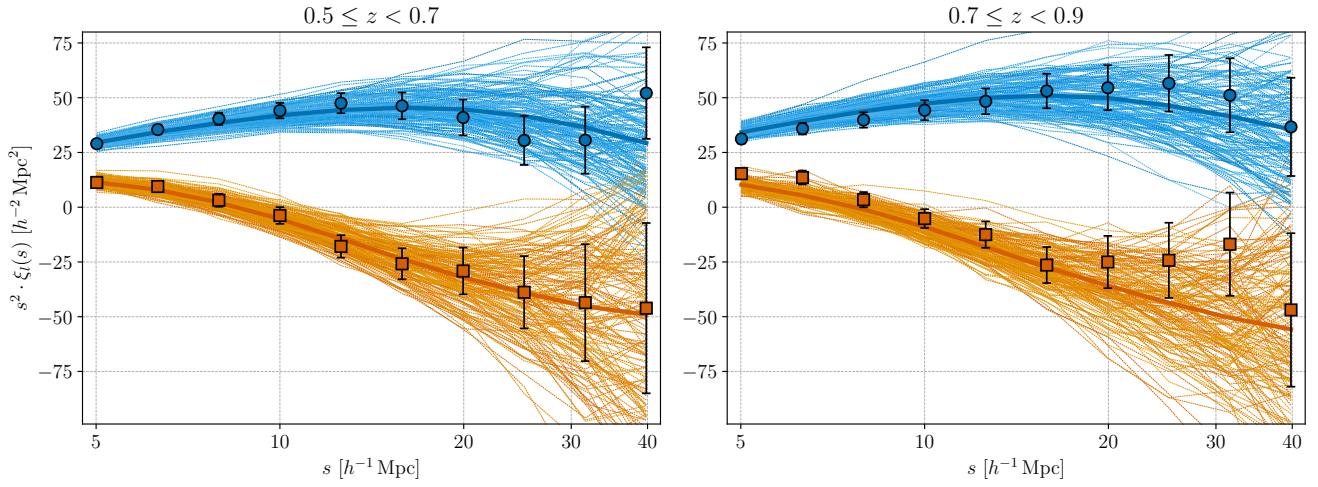


Figure 1. Monopole (blue circles) and quadrupole (orange squares) moments of the 2PCF measured from the G1 (left) and G2 (right) VIPERS sub-samples. The corresponding measurements from the 153 VIPERS mock catalogues are also plotted (thin solid lines), together with their average (thick solid line). The error bars on the data points correspond to the *rms* dispersion of the mocks. The consistency between the mocks and the real data highlights the very good fidelity in clustering properties of the mock galaxies.

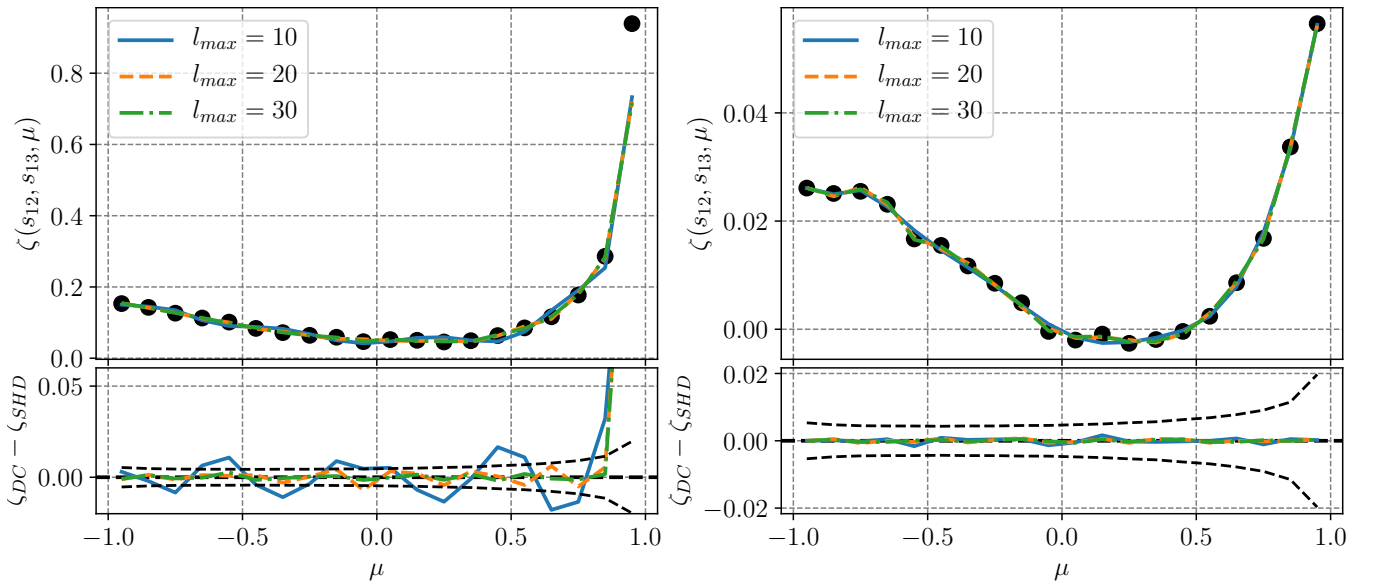


Figure 2. Top panels: estimates of the three-point correlation function for the G1 sample using both the triplet counting method (black dots) and the SHD method (solid lines), for different l_{max} as indicated by the legend (top panels). The left and right panels correspond to isosceles ($r_{12} = r_{13} = 10 h^{-1} \text{ Mpc}$) and non-isosceles ($r_{12} = 10 h^{-1} \text{ Mpc}$, $r_{13} = 30 h^{-1} \text{ Mpc}$) configurations, respectively. The bottom panels show the difference between the two estimators, for the different choices of l_{max} (solid lines). The dashed black curves correspond to $\pm 10\%$ of the statistical scatter of the mocks, highlighting the relative importance of the systematic errors introduced by the choice of l_{max} .

line of sight to the pair, measured at the midpoint of the separation vector itself.

We bin the pair counts using a constant logarithmic bin in s , $\Delta \log(s) = 0.1$, and a linear one for μ , $\Delta \mu = 0.05$, as in Pezzotta et al. (2017).

For each s bin we compute the 2PCF multipoles

$$\xi_l(s) = \frac{2l+1}{2} \int_{-1}^1 d\mu \mathcal{P}_l(\mu) \xi(s, \mu), \quad (5)$$

where $\mathcal{P}_\ell(\mu)$ are the Legendre polynomials. We only consider the

monopole $\ell = 0$ and quadrupole $\ell = 2$, since odd multipoles are zero by design, and the measured hexadecapole turns out to be consistent with zero within the (large) errors.

To validate our estimator, we measure the 2PCF multipoles for the subsamples of Table 1 and compare the results with those of previous VIPERS studies. Fig. 1 shows the 2PCF monopole and quadrupole moments of the VIPERS G1 and G2 samples (blue circles and the orange squares, respectively). The solid thin lines correspond to measurements of each mock catalogue, with the thicker line and errorbars on data points showing the average and *rms* of the

mocks respectively. This plot shows how the mock VIPERS samples reproduce faithfully the clustering of the real data, suggesting that they are adequate to estimate their errors and covariance. We have repeated the test using the P1 and P2 samples and verified that the results match those of Pezzotta et al. (2017, see Fig. 12)

The maximum separation considered in our analysis is set by the signal-to-noise of the 2PCF. The VIPERS footprint is highly elongated along the (equatorial) longitude, which significantly reduces the number of distant pairs in the transverse direction. As a result, the estimated quadrupole moment becomes noisy beyond $\sim 40 h^{-1}$ Mpc. We therefore set $s_{max} = 40 h^{-1}$ Mpc in our 2PCF analysis. In Sect. 7.1 we will also test the sensitivity of the results to the smallest separation scale considered, showing that the results are robust down to $s_{min} = 15 h^{-1}$ Mpc, which we then assume as the default value. In summary, our baseline range for the 2PCF analysis is $[15, 40] h^{-1}$ Mpc.

3.2 3PCF estimator

To measure the 3PCF of the VIPERS first data release catalogue (PDR1), Moresco et al. (2017) used the estimator of Szapudi & Szalay (1998) because of its ability to account for complicated survey geometry (Kayo et al. 2004). This estimator, however, is computationally demanding since it relies on brute-force galaxy triplet counting, whose computing time scales as $O(N^3)$. This becomes unbearable if applied to 153 mock catalogues with the size of VIPERS.

A major breakthrough in this respect has been the introduction by Slepian & Eisenstein (2015), of a more efficient estimator based on a spherical harmonics decomposition (hereafter SHD). For this algorithm, the computational cost scales as $O(N^2)$, making it successfully applicable to large galaxy samples such as the SDSS-DR12 CMASS catalogue (Slepian et al. 2017b). The method relies on the 3PCF Legendre polynomials expansion proposed by Szapudi (2004)

$$\zeta(s_{12}, s_{13}, \mu) = \sum_{l=0}^{l_{max}} \zeta_l(s_{12}, s_{13}) \mathcal{P}_l(\mu), \quad (6)$$

where the 3PCF $\zeta(s_{12}, s_{13}, \mu)$ is parametrized by two triangle sides s_{12}, s_{13} and their cosine angle $\mu = \cos(\hat{s}_{12} \cdot \hat{s}_{13})$. This expansion offers two advantages. The first one is that the multipole moments $\zeta_l(s_{12}, s_{13})$ can be efficiently estimated by locally expanding the density field at distances s_{12} and s_{13} in spherical harmonics and then by cross-correlating the expansion coefficients using the spherical harmonics addition theorem. The second advantage is that Eq. (6) typically requires a limited number of multipoles to converge. These properties dramatically reduce the computational cost, allowing us to measure the 3PCF in all VIPERS mocks and consider all triangle configurations. We refer the reader to Slepian & Eisenstein (2015) for a detailed description of the SHD estimator.

The main disadvantages of this estimator are that, for a given configuration, all triangles are mixed together; this is particularly relevant in all cases where the third side spans a large range of scales. For example, in the case of isosceles configurations with $s_{12} = s_{13}$, the third side s_{23} varies from 0 to $2 \times s_{12}$, i.e. well into the highly nonlinear regime, where theoretical predictions cannot be trusted. For this reason, here we will only consider triangles with all side lengths above a minimum value $s_{min} = 15 h^{-1}$ Mpc and up to a maximum length $s_{max} = 40 h^{-1}$ Mpc. This matches the scale used in the 2PCF analysis. In Sect. 7.2, we shall test the robustness of our results to such a choice.

3.2.1 Convergence of the SHD method

We first assess the sensitivity of the SHD method to the choice of l_{max} in Eq. 6. We thus compare the 3PCF of the G1 catalogue measured with the SHD method to that, supposedly exact, estimated with the same brute-force triplet counting technique used by Moresco et al. (2017). We show in Fig. 2 the results for two triangle configurations: isosceles triangles with $s_{12} = s_{13} = 10 h^{-1}$ Mpc (left panel) and non-isosceles triangles with $s_{12} = 10 h^{-1}$ Mpc and $s_{13} = 30 h^{-1}$ Mpc (right panel). In both cases, the same μ binning is used.

In the top panels, we compare the reference 3PCF measured with the triplet counting technique (black dots), with the one measured with the SHD method using $l_{max} = 10, 20$ and 30 (lines with different colours). These particular choice of configurations cover both the cases where highly non-linear scales are included (isosceles, left panel) or not (non-isosceles, right panel). In the bottom panels, we show the difference of the 3PCFs estimated with the two methods. As an indication of the relative value of the potential systematic error with respect to statistical errors, the black dashed lines indicate 10% of the *rms* scatter among the mock catalogues. For non-isosceles configurations (right panel), the SHD matches well the expected result, with differences of the order (or below) 1% of the random errors, almost independently of the choice of l_{max} . This implies that a limited number of multipoles ℓ is sufficient for Eq. (6) to converge to the correct result, typically $l < 10$.

On the contrary, the results of the SHD method for the isosceles configurations (left panel) depend on the choice of l_{max} and μ . For $l_{max} = 30$, the results are generally satisfactory (the difference between SHD and triplet counting is of the order of a few percent of the statistical error), except for $\mu = 1$, i.e. when $s_{23} \rightarrow 0$. This is not surprising, since elongated isosceles triangle shapes are difficult to reproduce in harmonics space.

Based on these results, we adopt a conservative approach in which: 1) we set $l_{max} = 30$ in the 3PCF estimate, and 2) we exclude the case $\mu = 1$ for isosceles configurations. We also choose to parameterise the 3PCF in terms of the three side lengths $\zeta(s_{12}, s_{13}, s_{23})$ instead of two sides and the cosine angle, $\zeta(s_{12}, s_{13}, \mu)$. Since the SHD method involves binning in the radial direction, we perform an additional step, described in Appendix A, to use the same binning along the three sides s_{12}, s_{13} and s_{23} .

Finally, we sort the triangles in increasing size $s_{12} \leq s_{13} \leq s_{23}$, to avoid repetitions. This choice also facilitates triangle selection: for example, we can exclude scales smaller than a chosen value by setting a threshold for one triangle side only.

3.2.2 Comparison with the 3PCF of mock samples

The second test is analogous to the one performed to validate the 2PCF estimator: we measure the 3PCF in the G1, G2, P1 and P2 VIPERS samples and compare the results with the same quantity measured in the mocks.

In Fig. 3 we show the results for the G1 and G2 samples (top and bottom panels, respectively). We detect a non-zero 3PCF signal up to the largest scales considered in our analysis, in agreement with Moresco et al. (2017). The VIPERS 3PCF agrees well with that of the mock samples, demonstrating that the VIPERS mocks are indeed adequate to estimate the errors for the 3PCF analysis, too.

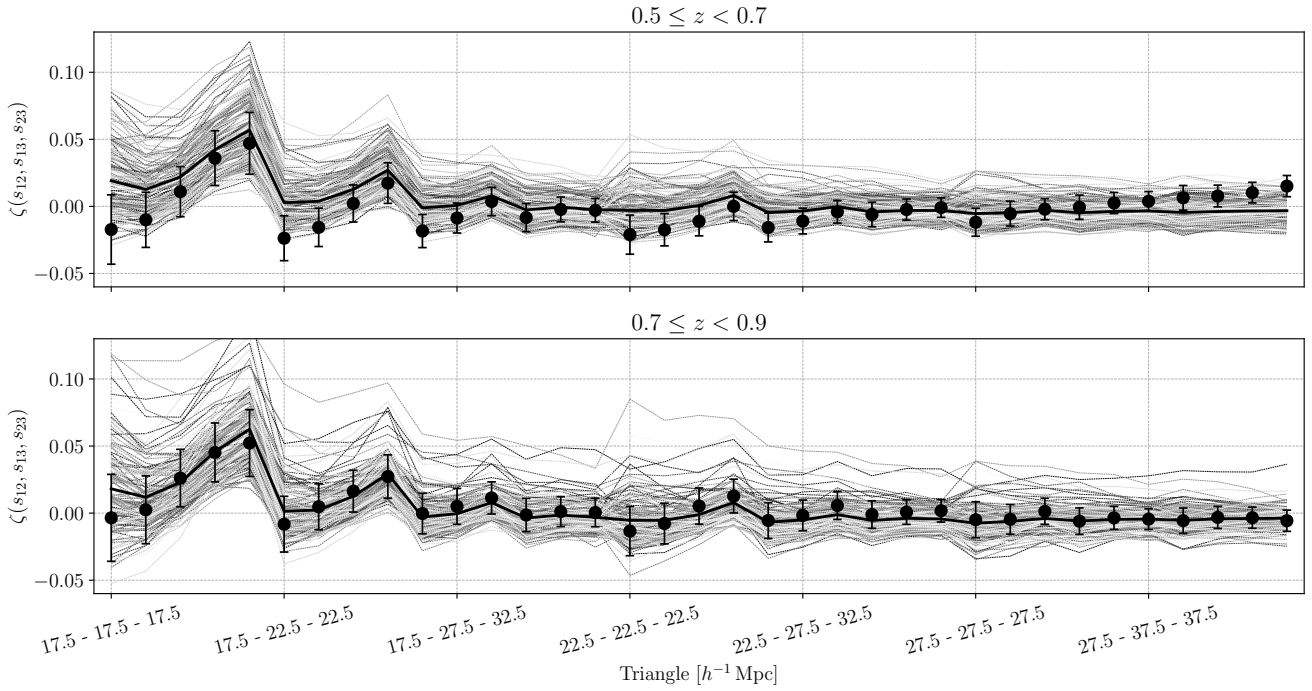


Figure 3. Monopole moments (black circles) of the three-point correlation function for the G1 and G2 samples (top and bottom panels, respectively), measured for some selected sets of triangles of different side lengths, as indicated on the x-axis. The corresponding measurements from the 153 VIPERS mock catalogues are also shown by the thin grey lines, together with their averages (solid black line). Error bars correspond to the *rms* scatter among the mocks.

4 COVARIANT ERRORS

To estimate the errors, we will not adopt an analytic, Gaussian model (like in, e.g., Slepian & Eisenstein 2017). Instead, supported by the results of the previous section, we directly estimate errors and their covariance matrix $C_{i,j}$ from the mock VIPERS catalogues, as

$$C_{i,j} = \frac{1}{N_m - 1} \sum_{k=0}^{N_m} (d_i^k - \bar{d}_i) (d_j^k - \bar{d}_j), \quad (7)$$

where d_i^k indicates the data vector in the i -th bin and in the k -th mock catalog. The size of the data vector and of the covariance matrix depend on the specific clustering analysis being performed. In the 2PCF analysis, performed in the range $15 \leq s_{min}^{2pt} \leq 40 h^{-1}$ Mpc, the size of the data vector is 10 and the corresponding 10×10 covariance matrix is shown in the lower left part of Fig. 4. For the 3PCF analysis, performed over the same range of scales, the size of the data vector is 35 and the covariance matrix corresponds to the upper-right part of the same figure. In the joint 2PCF and 3PCF analysis, the data vector has 45 elements and the covariance matrix, which also contains the 2PCF-3PCF cross-terms, corresponds to the full matrix of Fig. 4.

Both precision and accuracy of our covariance matrix depend on the number of mock catalogues used for its numerical estimation. Since this number is limited, a correction for the expected systematic errors should be considered (see, e.g. discussion in Hartlap et al. 2007; Percival et al. 2014). To this end, we follow Sellentin & Heavens (2016) in using a modified likelihood function, which we discuss in detail in Sect. 6.

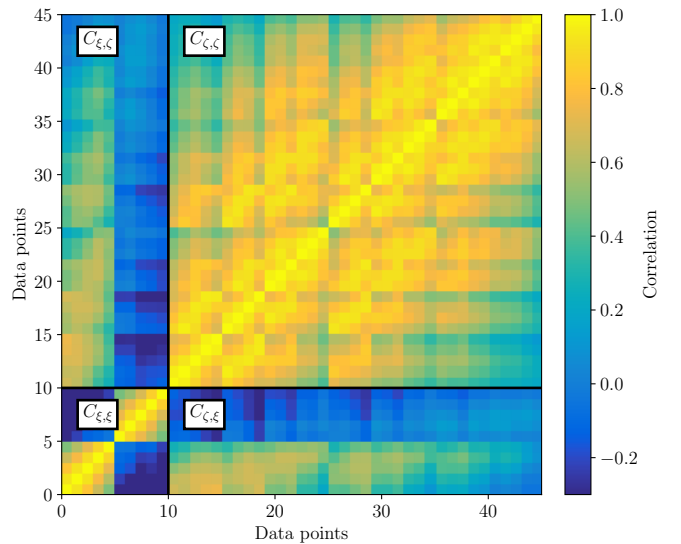


Figure 4. The global correlation matrix used in our joint likelihood analysis of the 2PCF and 3PCF, estimated from the 153 VIPERS mock catalogues using Eq. 7. We show here the one for the G1 sample, as an illustrative example. The matrix is composed by two sub-blocks, corresponding to the 2PCF monopole and quadrupole ($C_{\xi,\xi}$, bottom left), and the 3PCF monopole ($C_{\zeta,\zeta}$, top right), respectively, together with their cross-covariance ($C_{\xi,\zeta}$). The sub-arrays are used for the separate 2PCF and 3PCF analyses, while the full 45×45 matrix is used in the joint likelihood analysis.

5 MODELLING THE GALAXY 2- AND 3- POINT CORRELATION FUNCTIONS

In this section we describe our model for the anisotropic galaxy 2PCF,

$$\xi_g(s, \mu) = \langle \delta_g(\mathbf{x}) \delta_g(\mathbf{x} + \mathbf{s}) \rangle, \quad (8)$$

and 3PCF,

$$\zeta_g(s_{12}, s_{13}, s_{23}) = \langle \delta_g(\mathbf{x}) \delta_g(\mathbf{x} + \mathbf{s}_{12}) \delta_g(\mathbf{x} + \mathbf{s}_{13}) \rangle. \quad (9)$$

In these expressions, $\delta_g(\mathbf{x})$ is the galaxy density contrast at the position \mathbf{x} , while $\langle \dots \rangle$ indicates ensemble average.

The model relies on the approach of Scoccimarro et al. (1999); Scoccimarro (2004); McDonald & Roy (2009); Saito et al. (2014), and has already been used to perform 2PCF, 3PCF and joint 2PCF+3PCF analyses (Gil-Marín et al. 2015; de la Torre et al. 2017; Slepian & Eisenstein 2017).

5.1 Galaxy bias

The first ingredient of the model is the galaxy biasing relation of McDonald & Roy (2009)

$$\delta_g = b_1 \delta + \frac{b_2}{2} [\delta^2 - \langle \delta^2 \rangle] + \frac{b_{s^2}}{2} [s^2 - \langle s^2 \rangle] + O(\delta^3). \quad (10)$$

In this expression, the galaxy density contrast δ_g is a function of the matter non-linear over-density δ and of the non-local tidal field s^2 , which accounts for dependence of δ_g on the local potential ϕ (see e.g. Sect. II of McDonald & Roy 2009). The terms $\langle \delta^2 \rangle$ and $\langle s^2 \rangle$ guarantee that $\langle \delta_g \rangle = 0$. This bias model is then characterised by the four parameters $b_1, b_2, b_{s^2}, b_{3nt}$.

5.2 Distortion effects

Using the observed spectroscopic redshifts as a distance proxy introduces spurious distortions in the clustering properties that need to be accounted for. Three types of distortions need to be considered: those introduced by the departures from the Hubble flow, those induced by assuming an incorrect cosmological model in computing distances from redshifts and those due to the errors on the measured redshifts.

5.2.1 Peculiar motions

Peculiar velocities introduce a Doppler shift that modifies the mapping between spatial positions, \mathbf{x} , and the measured positions, \mathbf{s} :

$$\mathbf{s} = \mathbf{x} + \frac{v_{\parallel}}{aH(a)} \mathbf{e}_{\parallel} \quad (11)$$

where a is the expansion factor, v_{\parallel} is the radial component of the peculiar velocity vector, \mathbf{e}_{\parallel} is the unit radial vector, and \mathbf{s} is the redshift-space vector position of the object.

This mapping introduces a relation between the measured (redshift-space) galaxy over-density, $\delta_g(\mathbf{s})$, and the true, real-space one, $\delta_g(\mathbf{x})$

$$\delta_g(\mathbf{s}) = \left[1 + \delta_g(\mathbf{x}) \right] \left| \frac{d^3 s}{d^3 x} \right|^{-1}, \quad (12)$$

where $\left| \frac{d^3 s}{d^3 x} \right|^{-1}$ is the Jacobian of the map in Eq. (11).

In this work, we make the plane-parallel hypothesis, i.e. we assume that the relative separations between galaxy pairs are much smaller than the distance to the observer. This assumption is fully justified, since the maximum scale considered in our analyses ($40 h^{-1}$ Mpc) is much smaller than any distance to a VIPERS galaxy, which lies at $z \geq 0.5$. Under this approximation, Eq. (12) becomes

$$\delta_g(\mathbf{s}) = \frac{\delta_g(\mathbf{x}) + f \partial_{\parallel} \mathbf{u}}{1 - f \partial_{\parallel} \mathbf{u}}, \quad (13)$$

where the partial derivative is taken along the radial direction, \mathbf{u} is the peculiar velocity, and f is the linear growth rate of density fluctuations,

$$f = \frac{d \log D}{d \log a} \approx \Omega_M^{0.545}(z), \quad (14)$$

where $D(z)$ is the linear growth factor and the second relation is a good approximation in the flat Λ CDM model assumed here (see e.g. Wang & Steinhardt 1998; Huterer & Linder 2007).

5.2.2 Geometrical distortions

Choosing an incorrect fiducial cosmology to estimate distances from redshifts generates another kind of anisotropy, the well-known Alcock-Paczynski effect (Alcock & Paczynski 1979). The detection of this effect on intrinsically isotropic clustering features as the BAO peak in the 2PCF has been used to trace the expansion history of the Universe (Eisenstein et al. 2005; Kazin et al. 2013). Here, we will treat this effect as a nuisance to be marginalised over, since our analysis is limited to scales well below the BAO peak. As shown in de la Torre et al. (2017), the impact of this marginalisation in the error budget of the VIPERS clustering analysis is negligible. Therefore, we will set our fiducial cosmology equal to the flat Λ CDM model specified in Sect. 1 and safely ignore the Alcock-Paczynski effect.

5.2.3 Redshift measurement errors

Redshift measurement errors introduce a noise in the redshift-to-distance relation analogous to that of incoherent motions (Marulli et al. 2012), effectively erasing information on scales below

$$\sigma_{\pi} = \frac{c \sigma_z}{H(z)} h^{-1} \text{Mpc}, \quad (15)$$

where σ_z is the *rms* error typical of the adopted instrumental setup. For VIPERS, the errors are very well described by a Gaussian distribution with $\sigma_z = 5 \times 10^{-4} (1+z)$, corresponding to a length scale $\sigma_{\pi} \sim 1.5 h^{-1}$ Mpc (Scodreggio et al. 2018; Sereno et al. 2015).

5.3 2PCF model

To model the galaxy 2PCF we start from the matter power spectrum $P(k)$

$$\langle \delta(\mathbf{k}) \delta(\mathbf{k}') \rangle = 2\pi^3 \delta_D(\mathbf{k} - \mathbf{k}') P(|\mathbf{k}|). \quad (16)$$

Using Eq. (13) to account for redshift space distortions, we obtain an expression of the redshift-space power spectrum

$$P^S(k, \nu) = \int d^3 \mathbf{r} e^{-i\mathbf{k} \cdot \mathbf{r}} \left\langle e^{-i f k \nu \Delta u_{\parallel}} \left[\delta(\mathbf{x}) + f \partial_{\parallel} u_{\parallel}(\mathbf{x}) \right] \left[\delta(\mathbf{x}') + f \partial_{\parallel} u_{\parallel}(\mathbf{x}') \right] \right\rangle, \quad (17)$$

where $\nu = k_{\parallel}/k$, $u_{\parallel} = -v_{\parallel}/(f a H(a))$, v_{\parallel} and k_{\parallel} are the radial components of the peculiar velocity and wavenumber vectors, respectively, δ is the matter over-density, $u_{\parallel} = u_{\parallel}(\mathbf{x}) - u_{\parallel}(\mathbf{x}')$ and

$\mathbf{r} = \mathbf{x} - \mathbf{x}'$. The term in square brackets accounts for the effect of coherent motions that increase the clustering amplitude, whereas the exponential factor encodes the ‘‘Fingers of God’’ effect of incoherent motions. For a more detailed description, see [Taruya et al. \(2010\)](#).

Equation (17) is exact but of impractical use. Rather, using the approximations introduced by [Scoccimarro \(2004\)](#) and [Taruya et al. \(2010\)](#) for the case of biased mass tracers, we obtain the simpler expression

$$P_g^s(k, \nu) = D(\sigma_{12}, \sigma_z) \left[P_{\text{gg}}(k) + 2\nu^2 f P_{g\theta}(k) + \nu^4 f^2 P_{\theta\theta}(k) \right], \quad (18)$$

where

$$P_{\text{gg}}(k) = b_1^2 P_{\delta\delta}(k) + 2b_2 b_1 P_{b2,\delta}(k) + 2b_{s^2} b_1 P_{bs2,\delta}(k) + b_2^2 P_{b22}(k) + 2b_2 b_{s^2} P_{b2s2}(k) + b_{s^2}^2 P_{bs22}(k) + 2b_1 b_{3\text{nl}} \sigma_3^2(k) P_{\text{lin}}(k), \quad (19)$$

$$P_{g\theta}(k) = b_1 P_{\delta\theta}(k) + b_2 P_{b2,\theta}(k) + b_{s^2} P_{bs2,\theta}(k) + b_{3\text{nl}} \sigma_3^2(k) P_{\text{lin}}(k). \quad (20)$$

In these equations, $P_{\delta\delta}$, $P_{\delta\theta}$ and $P_{\theta\theta}$ are, respectively, the nonlinear matter density-density, density-(velocity divergence), and (velocity divergence)-(velocity divergence) power spectra. P_{lin} is the matter linear power spectrum, and $P_{b2,\delta}$, $P_{bs2,\delta}$, $P_{b2,\theta}$, $P_{bs2,\theta}$, P_{b22} , P_{b2s2} , P_{bs22} , σ_3^2 are 1-loop bias integrals; their expressions can be found in e.g. [Gil-Marín et al. \(2015\)](#); [de la Torre et al. \(2017\)](#). The linear and nonlinear power spectra of density and velocity divergence are specified at the effective redshift of the sample. To model P_{lin} we use the CAMB Boltzmann solver code ([Lewis et al. 2000](#)), whereas for $P_{\delta\delta}(k)$, $P_{\delta\theta}$, $P_{\theta\theta}$ we use the SPT 1-loop model of [Scoccimarro \(2004, Eqs. 63-65\)](#). In this model, the degree of non-linearity in $P_{\delta\delta}$, $P_{\delta\theta}$ and $P_{\theta\theta}$ is quantified by the same parameter that measures the clustering amplitude, i.e. $\sigma_8(z)$.

In Eq. (18) we have introduced the term $D(\sigma_{12}, \sigma_z)$ to model the combined damping effect of incoherent motions and redshift errors. Its explicit expression is

$$D(\sigma_{12}, \sigma_z) = \left(1 + k^2 \nu^2 \sigma_{12}^2 \right)^{-1} \cdot \exp \left(-k^2 \nu^2 \sigma_z^2 \right), \quad (21)$$

The first term, modelled as a Lorentzian damping, accounts for the effect of random motions within dark matter halos, quantified by the pairwise velocity dispersion σ_{12} . The second term accounts for the redshift measurement errors and is modelled as a Gaussian function. In our analysis, we fix σ_z to the VIPERS estimated value and leave σ_{12} as a free factor we can fit for and then treat it as a nuisance parameter.

Since the 2PCF model fits well the corresponding measurements from the VIPERS mocks on all scales considered, we decided to ignore the model correction terms $C_A(k, \nu, f, b_1)$ and $C_B(k, \nu, f, b_1)$ of [Taruya et al. \(2010\)](#), that are instead considered in other analyses (e.g. [Gil-Marín et al. 2015](#)).

To test the robustness of our model, we also considered an alternative 2PCF model, in which we used (1) the HALOFIT semi-analytical prescription calibrated by [Takahashi et al. \(2012\)](#) to model the matter power spectra and, (2) the fitting functions of [Bel et al. \(2019\)](#) to model $P_{\delta,\theta}(k)$ and $P_{\theta,\theta}(k)$. We find that the alternative model provide results very similar to the original one, the differences being much smaller than the statistical errors.

We then use Eq. (18) to model the multipole moments of the

anisotropic power spectrum

$$P_\ell^s(k) = \frac{2\ell + 1}{2} \int_{-1}^1 P_g^s(k, \nu) \mathcal{P}_\ell(\nu) d\nu \quad (22)$$

and, from these, the multipole moments of the anisotropic 2PCF

$$\xi_\ell^s(s) = i^\ell \int \frac{k^2}{2\pi^2} P_\ell^s(k) j_\ell(ks) dk, \quad (23)$$

where j_ℓ indicates the spherical Bessel functions. Having neglected the $C_A(k, \nu, f, b_1)$ terms, in our model the parameters b_1 and f are fully degenerate with σ_8 . The two bias parameters b_1 and b_2 are also highly degenerate.

5.4 3PCF model

The 3PCF model we adopt is the same one used by [Slepian & Eisenstein \(2017\)](#) and [Slepian et al. \(2017a\)](#) to detect the BAO feature in the 3PCF of SDSS DR12 galaxies and to measure their biasing relation in redshift space.

Our 3PCF model is derived from galaxy bispectrum $B(|\mathbf{k}_1|, |\mathbf{k}_2|, |\mathbf{k}_3|)$, defined as

$$\langle \delta_g(\mathbf{k}_1) \delta_g(\mathbf{k}_2) \delta_g(\mathbf{k}_3) \rangle = \delta_D(\mathbf{k}_1 + \mathbf{k}_2 + \mathbf{k}_3) B(|\mathbf{k}_1|, |\mathbf{k}_2|, |\mathbf{k}_3|). \quad (24)$$

In particular, we assume the redshift-space tree-level galaxy bispectrum derived in [Scoccimarro et al. \(1999\)](#). From this, we obtain the 3PCF model by Fourier transform, following the prescriptions of [Slepian et al. \(2017b\)](#).

The 3PCF model can be expressed as

$$\zeta(s_{12}, s_{13}, s_{23}) = \sum_{l=0}^{l=4} A_l(b_1, \gamma, \gamma', \beta) \cdot f_l(s_{12}, s_{13}, s_{23}) + B(b_1, \beta) \cdot \sum_{l=0}^{l_{\text{max}}} k_l(s_{12}, s_{13}, s_{23}), \quad (25)$$

where $\gamma \equiv b_2/b_1$ and $\gamma' \equiv b_{s^2}/b_1$ are combinations of the bias parameters. The first term of Eq. (25) accounts for contributions separable in k_1, k_2 in the [Scoccimarro et al. \(1999\)](#) bispectrum model. Its Fourier transform can be computed analytically as the product of two quantities. The first one, A_l , depends on the bias parameters, b_1, b_2, b_{s^2} , and on the linear distortion parameter $\beta = f/b_1$. The second one, f_l , depends on the linear power spectrum, $P_{\text{lin}}(k)$. The explicit expression of the A_l and f_l terms is given in Appendix B.

The second term in Eq. (25) accounts for the non separable terms (i.e. the terms in which k_3 appears explicitly). It is also made-up of two terms. The multiplicative factor $B = b_1^3(7\beta^2 + 2\beta^3)$ depends on b_1 and β while the terms $k_l(s_{12}, s_{13}, s_{23})$ in the sum depend on $P_{\text{lin}}(k)$. Their explicit expressions are given in Equations 17, 18 and 19 of [Slepian et al. \(2017b\)](#). The contribution of non-separable terms is small compared to that of the separable one and therefore we will ignore them in the 3PCF model, similarly to what we did with the C_A and C_B terms in the 2PCF model.

[Scoccimarro et al. \(1999\)](#); [Gil-Marín et al. \(2015\)](#) have modelled the effect of incoherent motions with a damping term in the galaxy bispectrum

$$D^B(\alpha\sigma_{12}) = \left\{ 1 + \alpha^2 \left[(k_1\nu_1)^2 + (k_2\nu_2)^2 + (k_3\nu_3)^2 \right]^2 \frac{\sigma_{12}^2}{2} \right\}^{-2}. \quad (26)$$

The magnitude of the damping effect is determined by the pairwise velocity dispersion, σ_{12} and modulated, in the model, by a multiplicative factor, α (with $\alpha = 0$ describing a purely coherent flow). In this work, however, we decided to drop this damping term since it has a negligible impact on scales larger than $10 h^{-1}$ Mpc as we show in a dedicated test in Sect. 7.2, where we assess the sensitivity of our results to the choice of s_{min} . This choice has the further advantage of avoiding computationally demanding 2-dimensional Fourier transforms.

5.5 Integral constraint

The so-called integral constraint effect originates from the assumption that the mean density estimated from the data coincides with the true one. This assumption biases the estimate of the correlation function on scales comparable to the size of the survey (Hui & Gaztañaga 1999), where it cannot be neglected, in particular at BAO scales (Slepian & Eisenstein 2017). However, the maximum scales considered in our analysis ($40 h^{-1}$ Mpc) are significantly smaller than the size of the survey. This guarantees that the integral constraint is negligible, as shown by Cappi et al. (2015), and will be ignored in our analysis.

5.6 Summary of model parameters

Our 2PCF and 3PCF models are specified by the set of free parameters listed in Table 2. These include: the clustering *rms* amplitude, σ_8 , the linear redshift distortion parameter $\beta \equiv f/b_1$, the pairwise velocity dispersion, σ_{12} , and the two galaxy bias parameters, b_1 and $\gamma \equiv b_2/b_1$.

The other model parameters that are kept fixed to their fiducial values are: the shape parameters of $P_{lin}(k)$ which are set to the Planck values (Planck Collaboration et al. 2020); the VIPERS *rms* redshift error, $\sigma_z = 5 \times 10^{-4}(1+z)$; the bias parameters b_{s2} and b_{3nl} , which are derived from local Lagrangian theory, i.e.

$$b_{s2} = -\frac{4}{7}(b_1 - 1), \quad (27)$$

$$b_{3nl} = \frac{32}{325}(b_1 - 1). \quad (28)$$

This choice is motivated by the fact that their measured values would be too noisy, as we have verified by running a dedicated likelihood analysis, aimed at testing the local Lagrangian bias hypothesis. Finally, we set $\alpha = 0$; a choice that has a negligible impact on the results, as we show in Sect. 7.2.

6 PARAMETER INFERENCE

To estimate the free parameters of the model, described as a vector θ , and their uncertainties, we compute the posterior probability, $P(\mu(\theta)|\mathbf{d})$, where $\mu(\theta)$ is the model prediction vector and \mathbf{d} is the data vector.

We perform three different analyses: one in which the data vector is represented by the VIPERS 2PCF monopole and quadrupole measured in the two samples G1 and G2 in the range $[15, 40] h^{-1}$ Mpc; one where we consider the measured 3PCF monopole of the same galaxies in the same range of scales; and one considering both statistics. In each case, we use the corresponding numerical covariance matrix C as described in Sect. 4.

To evaluate the posterior probability, we multiply the likelihood, $\mathcal{L}(\mathbf{d}|\mu, C)$, by the prior probability, $P(\theta)$. For each free

parameter, the prior is modelled as a step function with zero value outside the ranges specified in Table 2. To compute the likelihood $\mathcal{L}(\mathbf{d}|\mu, C)$, we use the covariance matrices described in Sect. 4. The latter have been numerically estimated from a large (153) but finite number of mock VIPERS catalogues, which introduces a systematic error. To correct for this, we adopt the approach of Sellentin & Heavens (2016) and use the modified likelihood function

$$\mathcal{L}(\mathbf{d}|\mu, C, N_m) = \bar{c}_p (\det C)^{-1/2} \left[1 + \frac{\chi^2(\mu, C)}{N_m - 1} \right]^{-\frac{N_m}{2}}, \quad (29)$$

where

$$\chi^2(\mu, C) = (\mathbf{d} - \mu)^T C^{-1} (\mathbf{d} - \mu) \quad (30)$$

$$\bar{c}_p = \frac{\Gamma\left(\frac{N_m}{2}\right)}{\pi(N_m - 1)^{p/2} \Gamma\left(\frac{N_m - \ell}{2}\right)}, \quad (31)$$

with N_m being the number of mock catalogues, and Γ the Gamma function.

To sample the posterior $P(\mu(\theta)|\mathbf{d})$ we use a Monte Carlo Markov Chain (MCMC) approach that generates a set of chains, i.e. collections of points in the parameter space $\{\theta_1, \theta_2, \dots, \theta_N\}$. Some of the parameters used in our analysis are expected to be (partly) degenerate. In these cases, we do not consider the individual parameters, but a suitable combination, as e.g. for $b_1\sigma_8$ and $f\sigma_8$ in the case of the 2PCF analysis alone.

7 RESULTS

In this section, we present the results of three analyses based, respectively, on the VIPERS 2PCF only, 3PCF only, and on the combination of the two statistics.

The first analysis is very similar to those of de la Torre et al. (2013, 2017); Pezzotta et al. (2017); Mohammad et al. (2018) and we use it to validate our likelihood pipeline. The main goal of the second analysis, which builds upon the work of Moresco et al. (2017), is to measure the bias parameters b_1 and $\gamma \equiv b_2/b_1$. Finally, the joint 2PCF and 3PCF analysis is aimed at breaking parameter degeneracies to obtain independent constraints on the galaxy bias, the evolution of cosmic structures and the clustering amplitude.

For all such analyses, the G1 and G2 VIPERS sub-samples are used (see Table 1). For the 2PCF study only, we also consider the P1 and P2 samples to allow us a direct comparison to Pezzotta et al. (2017).

7.1 2PCF

The results of the 2PCF analysis are shown in Fig. 5. In the panels we plot the 2D and 1D posterior probability distributions for the combinations of degenerate parameters $f\sigma_8$, $b_1\sigma_8$ and for σ_{12} , obtained from the analysis of the VIPERS P1 ($\bar{z} = 0.61$) and P2 ($\bar{z} = 0.87$) samples and for different s_{min} values indicated in the plots. We considered the 2PCF monopole and quadrupole moments and used the 10×10 covariance sub-matrix $C_{\xi, \xi}$ of Fig. 4.

Our analysis is very similar, though not identical, to that of Pezzotta et al. (2017). To minimize the differences, we compare our results obtained by using an SPT 1-loop 2PCF model in redshift space with their ‘‘TNS’’ model (Taruya et al. 2010). For the same reason, we push the analysis down to $s_{min} = 5 h^{-1}$ Mpc, but then show

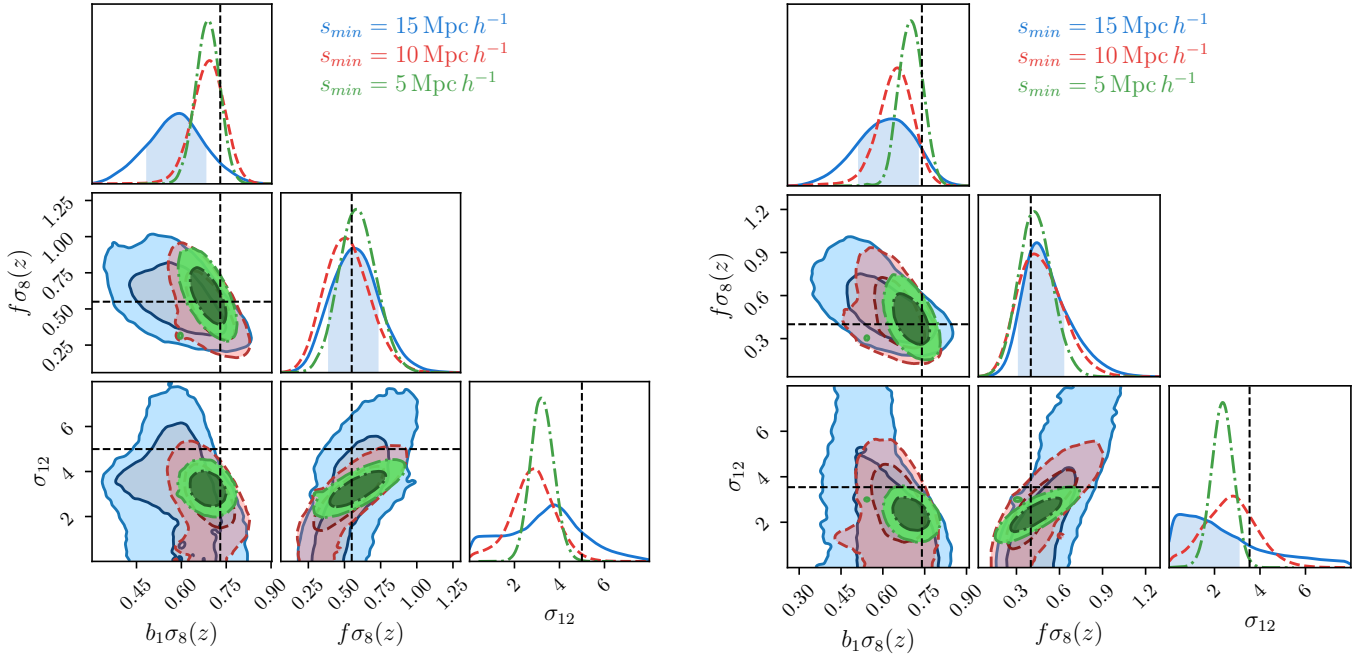


Figure 5. Marginalized 2D posterior probability levels for the parameters $b_1\sigma_8$, $f\sigma_8$ and σ_{12} , from the 2PCF analysis of the P1 and P2 “control” samples (left/right respectively), as a function of the minimum scale included in the analysis (see legend). The units of σ_{12} are h^{-1} Mpc and the darker/lighter shades for each set correspond to 68% and 95% confidence levels, respectively. 1D distribution functions on the diagonal give the 1D marginalized probability distributions of each parameter, with the 68% interval indicated by the blue-shaded area for the $s_{min} = 15 h^{-1}$ Mpc reference case only. The horizontal and vertical dashed lines give the best-fit values obtained by Pezzotta et al. (2017) on similar sub-samples of the VIPERS PDR2 catalogue.

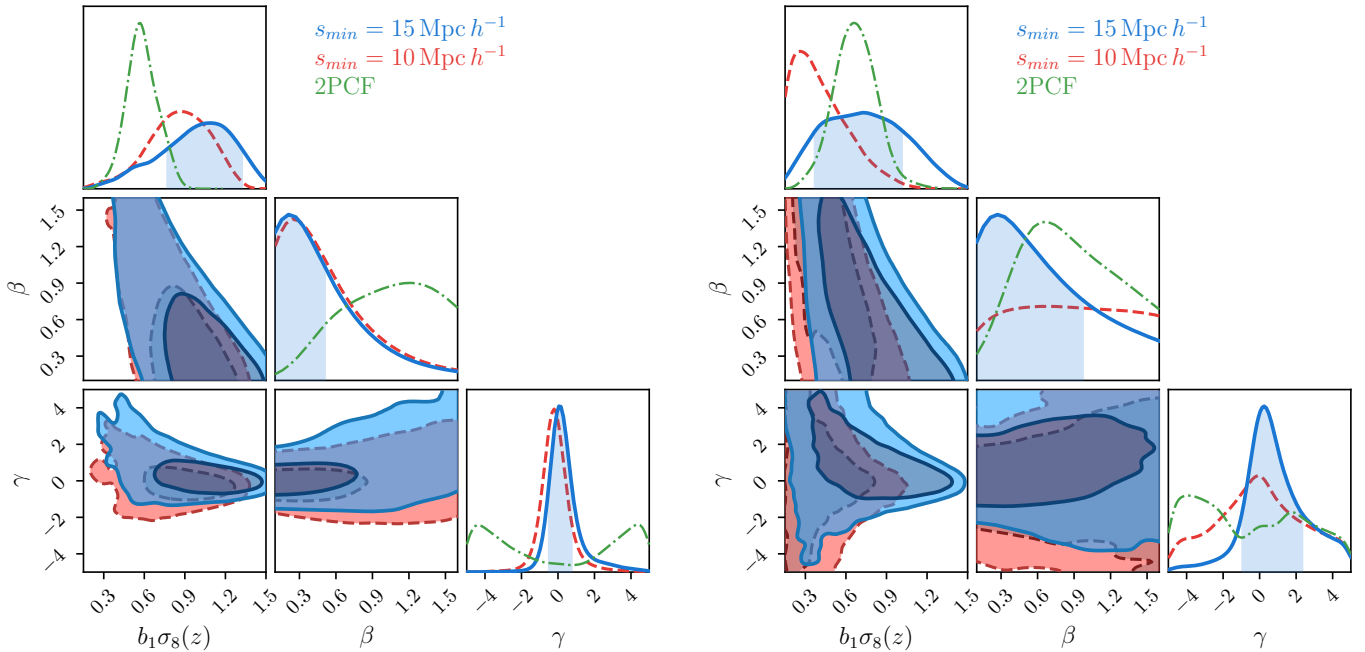


Figure 6. Marginalized 2D and 1D posterior distributions for the parameters $b_1\sigma_8$, β and γ , obtained from the 3PCF analysis of the G1 and G2 VIPERS samples (left and right panels, respectively). The plots show the results for the two choices of s_{min} as indicated by the legend. As in previous figures, darker/lighter shades correspond to 68 % and 95 % confidence levels, respectively. The green dashed lines report the marginalized 1D distributions obtained for the same parameters from the 2PCF analysis, using $s_{min} = 15 h^{-1}$ Mpc.

Table 2. Priors for the free parameters used in our likelihood analyses. The pairwise velocity dispersion, σ_{12} is expressed in h^{-1} Mpc.

Parameters Analysis	b_1	γ	β	$\sigma_8(z)$	σ_{12}
2PCF	[0.1, 5]	[-5., 5]	[0.1, 5]	[0, 5]	[0, 10]
3PCF	[0.1, 5]	[-5, 5]	[0.1, 5]	[0.1, 5]	–
2PCF+3PCF	[0.1, 5]	[-5, 5]	[0.1, 5]	[0, 5]	[0, 10]

the results obtained with larger values up to $s_{min} = 15 h^{-1}$ Mpc (our reference case).

The 2D and 1D posterior distributions shown in Fig. 4 agree well with the results of Pezzotta et al. (2017) except for the pairwise velocity dispersion, σ_{12} , which is significantly (2σ) smaller. This is not surprising since, as shown in Fig. 18 of Pezzotta et al. (2017), the Scoccimarro (2004) 2PCF model tends to underestimate the value of σ_{12} .

The 2D contours in Fig. 5 show a mild anti-correlation between $f\sigma_8$ and $b_1\sigma_8$, which is expected since larger redshift distortions that boost up the 2PCF monopole can be compensated by reducing the clustering amplitude $b_1\sigma_8$. In addition, we find a positive correlation between $f\sigma_8$ and σ_{12} , which is explained by the fact that damping effects can be compensated by increasing the clustering amplitude.

To assess the sensitivity of our results to some of the model parameters, we have performed two robustness tests. In the first one we have repeated the likelihood analysis with different values of $s_{min} = 5, 10$ and $15 h^{-1}$ Mpc. The results are shown in the same Fig. 5. As expected, increasing the value of s_{min} amplifies the errors, especially for the nonlinear σ_{12} parameter. However, no systematic error is introduced as all results agree with those of Pezzotta et al. (2017) and with each other.

As a second test we used the alternative 2PCF model introduced in Sect. 5.3 in which we 1) use HALOFIT (Takahashi et al. 2012) to model $P_{\delta\delta}$ and 2) adopt the fitting formula of Bel et al. (2019) to model $P_{\delta\theta}$ and $P_{\theta\theta}$. The results are very similar to those obtained with the reference 2PCF model.

Finally, we have repeated the likelihood analysis on G1 and G2 samples that we use for the 3PCF analysis too. The results, which are qualitatively similar to those obtained with P1 and P2, are summarized in Table 7.3 where we list the best-fit parameters and their 1σ uncertainties.

We confirm that the 2PCF analysis successfully constrains the parameter combinations $f\sigma_8$, $b_1\sigma_8$ and $\beta \equiv f/b_1$ but leave γ unconstrained. This is not surprising since this parameter is sensitive to the small scale clustering that we ignore, having set $s_{min} = 15 h^{-1}$ Mpc. Indeed, when the analysis is extended down to $s_{min} = 5 h^{-1}$ Mpc, we do measure a γ value significantly different from zero, yet mildly inconsistent with the results of previous VIPERS analyses (Cappi et al. 2015; Di Porto et al. 2016). This value is also in tension with the one yielded by the 3PCF analysis presented in the next section. It probably indicates the minimum scales below which our galaxy 2PCF model fails and thus justifies our choice of setting $s_{min} = 15 h^{-1}$ Mpc.

7.2 3PCF

We have repeated the likelihood analysis to compare the 3PCF measurements in the G1 and G2 sample with the 3PCF model described in Sect. 5.4 and the 25×25 covariance matrix $C_{\zeta,\zeta}$ shown in Fig. 4.

This analysis improves upon the one performed by Moresco

et al. (2017) in different ways. First, we use a more accurate 3PCF model and a covariance matrix estimated from realistic mock catalogues to perform a full likelihood analysis. Secondly, here we use the final, PDR2 release of the VIPERS catalogue. Finally, we consider all triangle configurations and not just a few subsets. We stress the importance of this latter aspect since, in our estimator, we use a triangle representation that is flexible enough to allow us to select subsets of triangles characterized by specific configurations and side lengths, greatly simplifying the comparison with model predictions.

The plots in Fig. 6 are analogous to those of Fig. 5. They show the 2D and 1D marginalized posterior distributions for the parameters $b_1\sigma_8$, β and γ obtained from the 3PCF measured in the G1 (left) and G2 (right) samples. The best-fitting parameters and their uncertainties are listed in Table 7.3. The 3PCF analysis allows us to estimate the nonlinear bias parameter γ , which turns out to be consistent with zero, while 2PCF is completely insensitive to it, as shown by the green, dot-dashed curves in the bottom right panels. This result is in agreement with Moresco et al. (2017) and marginally consistent with those obtained from counts-in-cells analyses of Cappi et al. (2015) and Di Porto et al. (2016) where a non-zero value of γ was measured but on scales much smaller than those considered here.

The constraints on the distortion parameter β are, on the contrary, quite weak. The best-fit value of this parameter is consistent with zero within the errors. This is not unexpected since in our analysis we considered only the 3PCF monopole moment, which is insensitive to the RSD effects. Constraints on β could be obtained by considering the 3PCF multipoles. This is, however, beyond the scope of this work since a multipole analysis would require the use of a significantly larger covariance matrix, which cannot be accurately estimated with the 153 mock catalogues at our disposal.

Another interesting feature is the mild degeneracy between β and the clustering amplitude $b_1\sigma_8$ also seen for the 2PCF. The difference is that here the error on $b_1\sigma_8$ from the 3PCF analysis is about 3 times larger than from the 2PCF one.

To test the sensitivity to the choice of s_{min} we repeated the likelihood analysis using $s_{min} = 5, 10, 15$ and $20 h^{-1}$ Mpc. In Figure 6 we only show the cases of $s_{min} = 10$ and $15 h^{-1}$ Mpc to avoid overcrowding. When s_{min} decreases, the maximum of the 1D posterior distributions for $b\sigma_8$ shifts to smaller values. However, due to the large errors, the best-fit values of $b\sigma_8$ (but also the ones of γ and β) are in fact consistent with each other for all choices of s_{min} . In Appendix C we present a more detailed study of the impact of s_{min} on the parameters' estimates using the VIPERS mock catalogues.

Finally, despite their different shapes, the 1D posteriors of all parameters obtained from the 3PCF analysis for all values of s_{min} largely overlap those obtained from the 2PCF.

To further assess the impact of nonlinear effects, we compared the measured 3PCF with a model including the damping term of Eq. (26) and varying its strength. The result is shown in Fig. 7, with the reference case with $\alpha = 0$ corresponding to no damping. We set the pairwise velocity dispersion, σ_{12} , equal to the best fit

value obtained from the 2PCF analysis. The plot compares model predictions with the 3PCF measured for various triangle shapes, whose side lengths are indicated on the x-axis. The results show that incoherent motions do not significantly affect model predictions on the scales considered in our analysis. They may, however, become relevant for next-generation surveys, in which statistical errors will be significantly smaller than those considered here. We plan to further investigate this aspect and introduce a novel nonlinear 3PCF model to tackle the problem.

7.3 Joint analysis of 2PCF and 3PCF

Finally, we perform for the first time a joint 2PCF and 3PCF correlation analysis on the VIPERS data. The main goal is to break the parameter degeneracy and obtain individual estimates for σ_8 , for the linear growth rate f , and for the two bias parameters b_1 and γ . Fig. 8 shows the 1D and 2D posterior probability distributions (blue regions and solid curves) of these parameters from the likelihood analysis of the G1 and G2 samples and using the full 45×45 covariance matrix. The same range of scales $[15, 40] \text{ Mpc } h^{-1}$ was considered in both the 2- and 3-point statistics. The 1D posterior distributions obtained from the 2PCF-only (green, dot-dashed) and 3PCF-only (red, dashed) analyses are also shown for reference. The best-fit values of the joint analysis and their uncertainties are listed in Table 7.3.

The joint analysis successfully breaks the $\sigma_8 - b_1 - f$ degeneracy, and the parameters can be measured individually, although with different uncertainties. The value of σ_8 is measured with a $\sim 20\%$ uncertainty in both G1 and G2 samples. The error on b_1 is $\sim 20\%$ in the G1 sample, increasing to $\sim 30\%$ in G2. The error on the growth rate f is significantly larger ($65 - 75\%$), reflecting the fact that the $f - \sigma_8$ degeneracy is only partially broken by our analysis. Though significantly less precise, it is reassuring that our best-fit σ_8 and f values are in agreement with those of the [Planck Collaboration et al. \(2020\)](#) cosmology, scaled to the redshift of the survey (vertical and horizontal dashed lines). The sensitivity of these results to the choice of s_{min} is thoroughly discussed in Appendix C.

The joint analysis does not improve the estimate of γ , whose precision is driven by the 3PCF signal, as shown in Fig. 8. It does instead improve the estimate of σ_{12} whose value, in agreement with the one obtained from the 2PCF analysis, is estimated with a significantly higher precision.

Overall, the results of the joint analysis clearly show that the degeneracy of some parameters are successfully broken, thanks to the ability to extract information from intermediate to small scales where nonlinear effects are relevant, both in the evolution of the density fluctuation and in the biasing relation.

8 DISCUSSION AND CONCLUSIONS

In this work, we have measured the 2PCF and 3PCF of the galaxies in the final data release of the VIPERS survey and used their joint information to break parameter degeneracies and estimate the galaxy bias parameters, b_1 and γ , the clustering amplitude, σ_8 , and the linear growth rate of density fluctuations, f , at two redshifts $z \simeq 0.61$ and $z \simeq 0.8$.

Because of the survey footprint, separated in two patches highly elongated in one direction, we performed the analysis in configuration space focusing on scales smaller than $40 h^{-1} \text{ Mpc}$. To do so, we adopted a 1-loop anisotropic 2PCF model to account for nonlinear effects, galaxy bias and redshift distortions. For the 3PCF we

considered the tree-level model of its monopole moment in redshift space proposed by [Slepian et al. \(2017b\)](#). To estimate the 3PCF we have used the SHD method of [Slepian & Eisenstein \(2015\)](#) whose efficiency allowed us to measure the 3PCF of all 153 mock VIPERS catalogs and thus to estimate the covariance matrix used in the likelihood analysis. Because of all these aspects, we believe that our analysis improves over the previous joint 2PCF and 3PCF analysis of the WiggleZ galaxy sample that was performed by [Marín et al. \(2013\)](#) using the brute-force triplet counting estimator simplified analytic models for 2PCF, 3PCF and their covariance matrix.

The main results of this work can be summarised as follow:

- The results of our 2PCF analysis agree, as expected, with those obtained by [Pezzotta et al. \(2017\)](#) in the range $[5, 50] h^{-1} \text{ Mpc}$ despite having used a different covariance matrix and a different 2PCF model. Indeed, our estimates of

$$f\sigma_8(z = 0.61) = 0.58 \pm 0.12$$

$$f\sigma_8(z = 0.87) = 0.43 \pm 0.12$$

and

$$b_1\sigma_8(z = 0.61) = 0.69 \pm 0.04$$

$$b_1\sigma_8(z = 0.87) = 0.70 \pm 0.04$$

match those of [Pezzotta et al. \(2017\)](#) ($f\sigma_8(z = 0.61) = 0.55 \pm 0.12$, $f\sigma_8(z = 0.87) = 0.40 \pm 0.11$; $b_1\sigma_8(z = 0.61) = 0.73 \pm 0.03$, $b_1\sigma_8(z = 0.87) = 0.74 \pm 0.04$).

When we consider pairs with $s_{min} \geq 10 h^{-1} \text{ Mpc}$ the 1D posterior probability distribution of $\gamma \equiv b_2/b_1$ is flat, whereas it peaks at negative values when pairs at separations as small as $5 h^{-1} \text{ Mpc}$ are included. Since a negative value is neither confirmed by previous VIPERS analyses ([Cappi et al. 2015](#); [Di Porto et al. 2016](#)) nor by our joint 2PCF and 3PCF analysis, we consider it as a piece of evidence that the 2PCF model is inadequate to describe galaxy clustering on such small scales. Moreover, we found that including pairs with separations larger than $40 h^{-1} \text{ Mpc}$, where shot noise starts to be significant, increases the computational cost of a less accurate covariance matrix and does not improve the quality of the fit.

For all these reasons, we focused on a smaller scale range $[15, 40] h^{-1} \text{ Mpc}$, and then assessed the robustness of our results to this choice. We then repeated the 2PCF analysis of G1 and G2 samples using this range and found $f\sigma_8(z = 0.61) = 0.47^{+0.17}_{-0.15}$. This is in good agreement with the estimates of [de la Torre et al. \(2017\)](#), $f\sigma_8(z = 0.6) = 0.48 \pm 0.11$, and of [Gil-Marín et al. \(2017\)](#), $f\sigma_8(z = 0.57) = 0.432 \pm 0.022$. Our measurements are shown in Fig. 9 together with existing estimates of $f\sigma_8$ obtained at different redshifts. As evident, there is an excellent agreement with previous results and with the theoretical expectation of a Planck cosmology ([Planck Collaboration et al. 2020](#)).

- We measured the 3PCF of the G1 and G2 samples in the same range as the 2PCF, $[15, 40] h^{-1} \text{ Mpc}$, for all triangle configurations. We compared these measurements with the model predictions to estimate the bias parameters b_1 and γ (for the remaining parameters we have assumed a local Lagrangian bias model). We found $\gamma(z = 0.61) = 0.1^{+0.8}_{-1.3}$ and $\gamma(z = 0.8) = 0.2^{+3.5}_{-1.3}$, in tension with the result of [Moresco et al. \(2017\)](#) ($\gamma(z \simeq 0.6) = -0.47 \pm 0.144$). The mismatch probably reflects the different scales probed by the two cases, since [Moresco et al. \(2017\)](#) pushed their analysis to scales as small as $1 h^{-1} \text{ Mpc}$ (and fixed all parameters of the model except b_1 and b_2).

[Di Porto et al. \(2016\)](#) estimated the biasing function from a count-in-cells analysis of the first data release of VIPERS. Among the

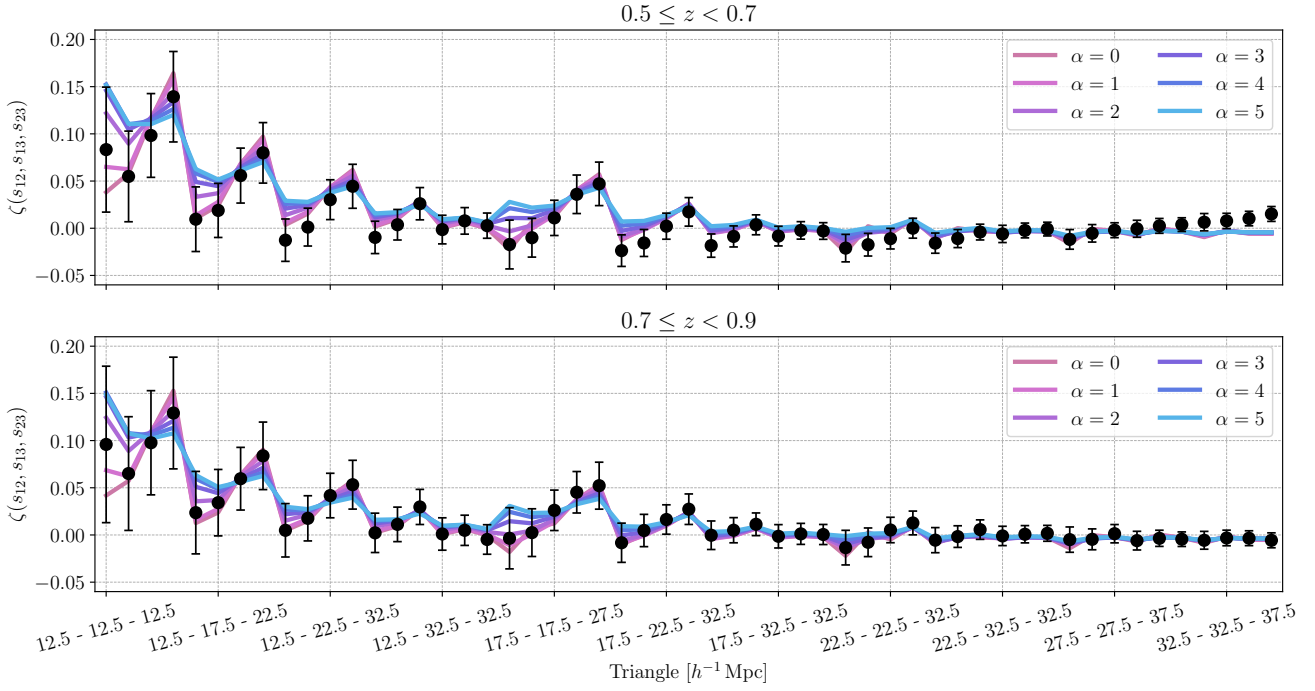


Figure 7. The impact of small-scale damping on our model for the 3PCF monopole. The estimated 3PCF from the VIPERS G1 and G2 samples (top and bottom respectively, data and error bars as in Fig. 3) are compared to the theoretical predictions, varying the amplitude of nonlinear motions, through the parameter α . The case $\alpha = 0$ corresponds to the reference case, in which small-scales nonlinear motions are ignored.

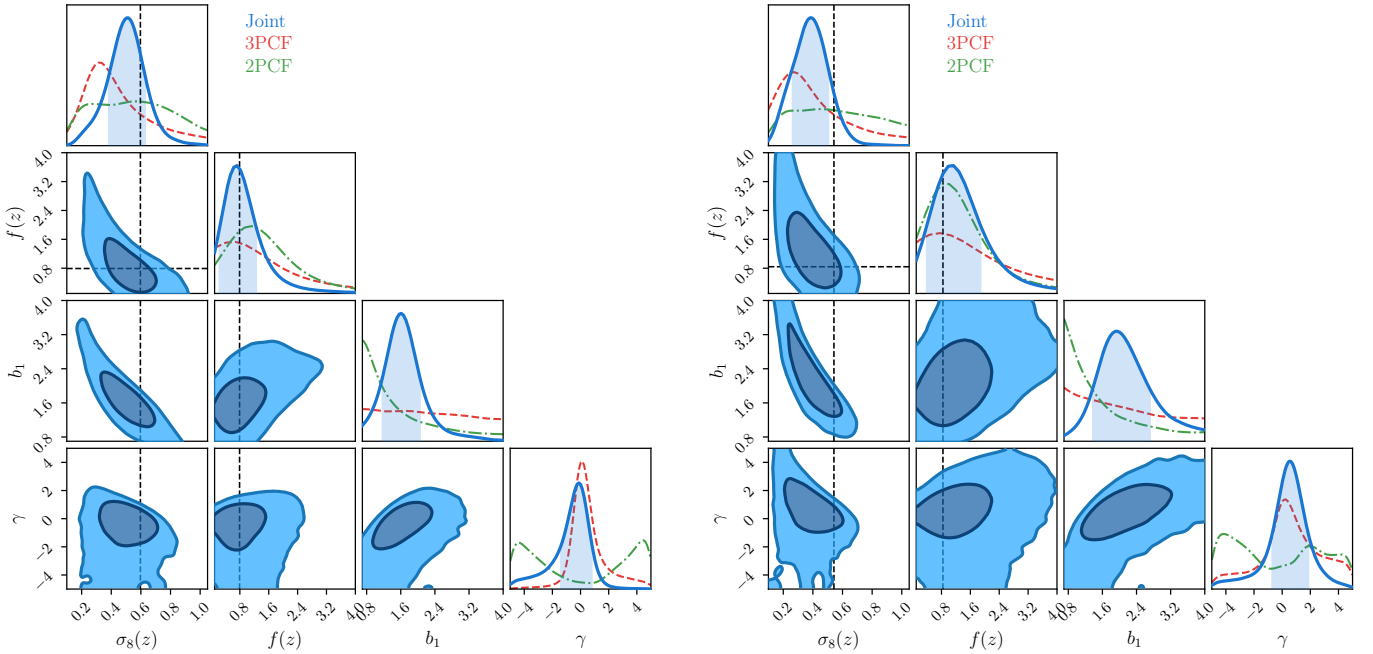


Figure 8. Marginalized 1D and 2D posterior distributions for the parameters $\sigma_8(z)$, $f(z)$ and b_1 , from the joint 2PCF+3PCF analysis of the G1 and G2 VIPERS samples (left and right panels, respectively). All estimates use $s_{min} = 15 h^{-1} \text{Mpc}$. The meaning of contours and shaded areas are as in Fig. 6. The vertical and horizontal black dashed lines show for reference the values measured for the same parameters by Planck Collaboration et al. (2020), self-consistently scaled to the corresponding VIPERS redshift.

Table 3. Summary of the best-fit parameter values and their 1σ uncertainties, as obtained from the G1/G2 VIPERS samples using the 2PCF-only, 3PCF-only and joint 2PCF+3PCF analyses. The parameters common to all analyses are b_1 , γ , β , σ_8 . For the 2PCF and joint analyses, the pairwise velocity dispersion σ_{12} is also considered. To account for parameter degeneracy, we also list some of the relevant parameter combinations constrained by the individual 2PCF and 3PCF analyses.

Sample	Probe	$\sigma_8(z)$	b_1	γ	β	σ_{12}	f	$b_1\sigma_8(z)$	$f\sigma_8(z)$
G1	2PCF	–	–	–	1.2 ± 0.6	2.4 ± 2.1	–	$0.56^{+0.12}_{-0.11}$	0.7 ± 0.2
	3PCF	–	–	$0.1^{+0.8}_{-1.3}$	$0.02^{+0.70}_{-0.0}$	–	–	1.0 ± 0.3	0.0 ± 0.5
	Joint	0.50 ± 0.12	1.60 ± 0.43	$-0.1^{+0.8}_{-1.3}$	$0.4^{+0.3}_{-0.2}$	2.4 ± 2.0	$0.64^{+0.55}_{-0.37}$	$0.84^{+0.09}_{-0.14}$	$0.36^{+0.17}_{-0.12}$
G2	2PCF	–	–	–	$0.6^{+0.9}_{-0.3}$	$1.0^{+1.6}_{-1.0}$	–	$0.67^{+0.15}_{-0.17}$	$0.49^{+0.42}_{-0.16}$
	3PCF	–	–	$0.2^{+3.5}_{-1.3}$	$0.0^{+1.4}_{-0.0}$	–	–	$0.4^{+0.5}_{-0.2}$	$0.0^{+0.7}_{-0.0}$
	Joint	$0.39^{+0.11}_{-0.13}$	$1.9^{+0.8}_{-0.5}$	$0.5^{+1.3}_{-1.2}$	$0.49^{+0.31}_{-0.23}$	$1.0^{+1.6}_{-1.0}$	1.0 ± 1.0	$0.74^{+0.07}_{-0.08}$	$0.43^{+0.16}_{-0.15}$

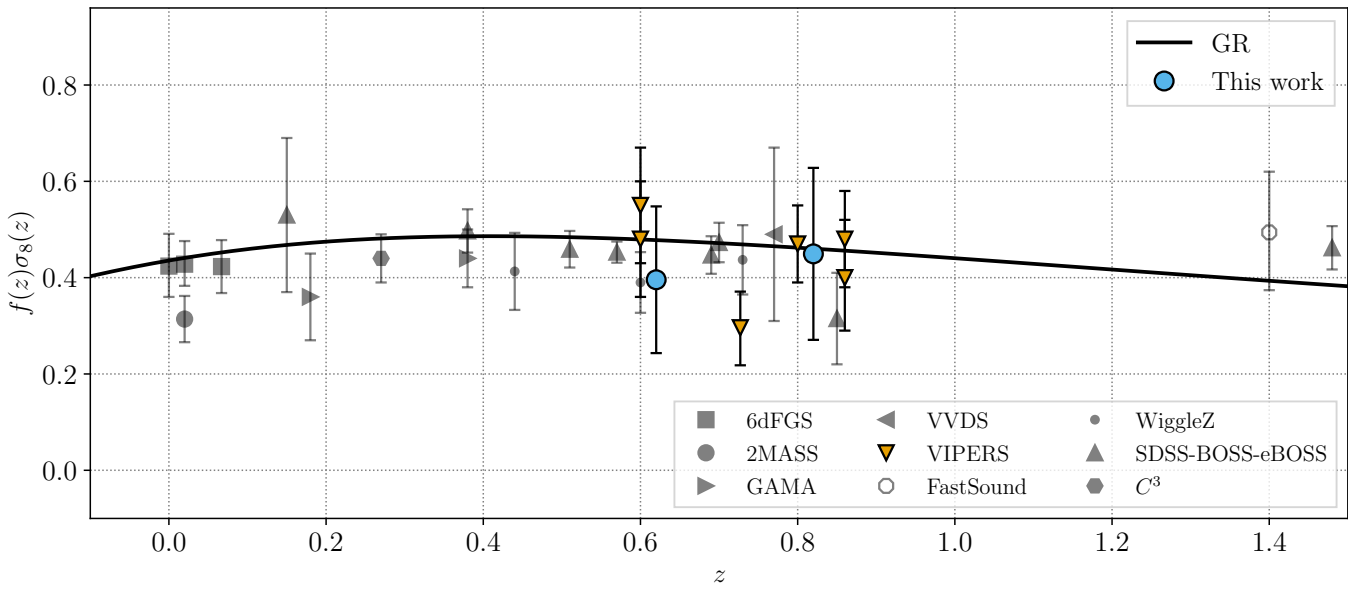


Figure 9. Comparison of our new estimates of the growth rate of structure, parameterised by the product $f\sigma_8$ (light blue circles), with previous measurements from the literature: 6dFGS (Beutler et al. 2012; Huterer et al. 2017; Adams & Blake 2017); 2MASS (Davis et al. 2011); GAMA (Blake et al. 2013); WiggleZ (Blake et al. 2012); VVDS (Guzzo et al. 2008); VIPERS (de la Torre et al. 2013, 2017; Pezzotta et al. 2017; Hawken et al. 2017; Mohammad et al. 2018); FastSound (Okumura et al. 2016); SDSS+BOSS+eBOSS (eBOSS Collaboration et al. 2020), "C³ - Cluster clustering cosmology" (Marulli et al. 2020). The black solid line shows the Λ CDM + GR Planck Collaboration et al. (2020) model prediction.

shape parameters are used to characterize the biasing function in that analysis the one dubbed $B \equiv [1 - \tilde{b}/\tilde{b}]$, can be directly compared to γ . The measured B values at the redshifts of the G1 and G2 samples and on the scale of $8 h^{-1}$ Mpc ($B(z = 0.6) = 0.007 \pm 0.006$ and $B(z = 0.8) = 0.005 \pm 0.005$) agree with our estimates of γ ,

Cappi et al. (2015) also performed counts in cells to derive volume-averaged higher-order correlation functions from which they inferred the bias parameters b_1 and b_2 . The scales considered in their analyses and the magnitude cuts are, however, different from ours. Nevertheless, it is reassuring that, similarly to our case, they did not detect significant deviations from a linear biasing.

- We have shown that a joint 2- and 3-point correlation analysis of the VIPERS samples successfully breaks the degeneracy among σ_8 , f and b_1 (and, consequently, b_2) and reduces the errors in the estimate of their combinations $f\sigma_8$, $b_1\sigma_8$ and f/b_1 . It is instructive to compare our results to those of similar analyses, aimed at breaking parameter degeneracies by combining 2- and 3-point statistics in configuration (Marín et al. 2013) and Fourier space (Gil-Marín

et al. 2017) and by combining clustering and gravitational lensing measurements using the VIPERS PDR2 data (de la Torre et al. 2017).

Our estimates of the clustering amplitude, $\sigma_8(z = 0.61) = 0.50 \pm 0.12$ and $\sigma_8(z = 0.8) = 0.39^{+0.11}_{-0.13}$, are in good agreement with those obtained by de la Torre et al. (2017) ($\sigma_8(z = 0.6) = 0.52 \pm 0.06$ and $\sigma_8(z = 0.86) = 0.48 \pm 0.04$), Marín et al. (2013) ($\sigma_8(z = 0.55) = 0.61^{+0.08}_{-0.09}$), Gil-Marín et al. (2017) ($\sigma_8(z = 0.57) = 0.66 \pm 0.067$) and with the Planck Λ CDM predictions, as shown in the right panel of Fig. 10.

Similarly, our estimates of the growth rate $f(z = 0.61) = 0.64^{+0.55}_{-0.37}$ and $f(z = 0.8) = 1.0 \pm 1.0$ agree with those of de la Torre et al. (2017) ($f(z = 0.6) = 0.93 \pm 0.22$ and $f(z = 0.86) = 0.99 \pm 0.19$) and Gil-Marín et al. (2017) ($f(z = 0.57) = 0.649 \pm 0.076$) within the error that is much larger in our case. All these measurements are shown in the left panel of Fig. 10 together with the Planck Λ CDM predictions (Planck Collaboration et al. 2020).

We notice that the errors on both f and σ_8 in our case are signif-

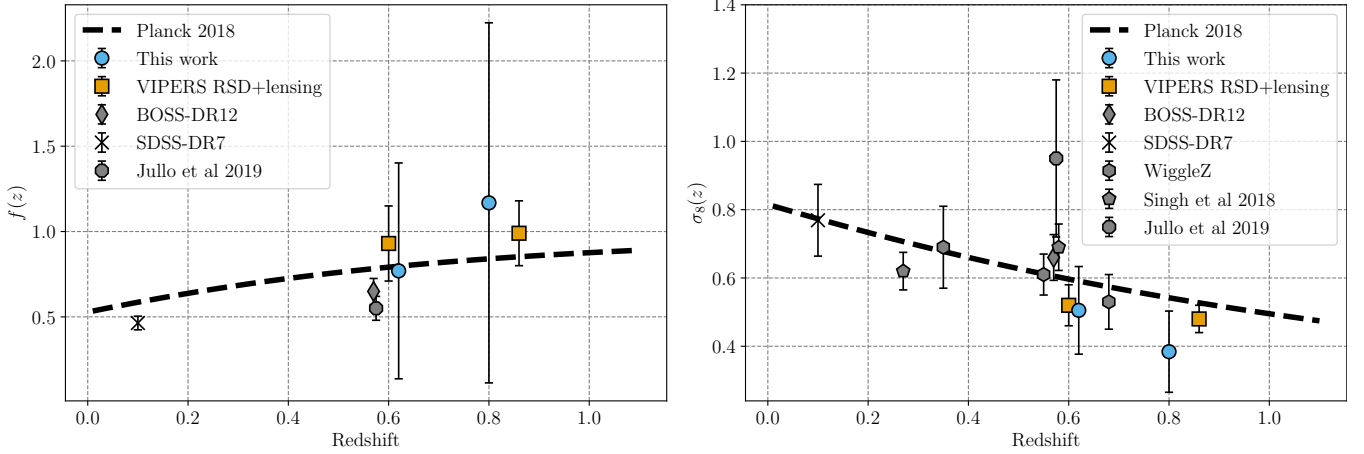


Figure 10. Values for $f(z)$ (left panel) and $\sigma_8(z)$, as estimated from our joint 2PCF and 3PCF analysis (light blue circles), again compared to other recent measurements using different techniques: VIPERS joint lensing-RSD analysis (de la Torre et al. 2017), BOSS-DR12 (Gil-Marín et al. 2017), Wiggle-z (Marín et al. 2013). For completeness, we also include results at smaller redshifts by Shi et al. (2018), Singh et al. (2019) and Jullo et al. (2019).

icantly larger than in de la Torre et al. (2017), despite having used similar datasets. The reason for this is twofold. First of all, we have adopted a more conservative approach and considered $s_{min} = 15 h^{-1}$ Mpc, whereas de la Torre et al. (2017) used $s_{min} = 5 h^{-1}$ Mpc. This choice, motivated by the discrepant γ value found in the 2PCF analysis, prevents us from accessing information encoded on smaller scales. If these are included, then the errors in the measured f and σ_8 significantly decrease towards values comparable to those of de la Torre et al. (2017), as illustrated in Appendix C. The second reason is that the clustering-lensing analysis is more efficient in breaking parameter degeneracy than the joint 2PCF-3PCF. In fact, the latter combines the galaxy 2PCF, which has a $b_1\sigma_8$ degeneracy, to the galaxy 3PCF, which has a similar degeneracy, $b_1^3\sigma_8^4$. On the contrary, the lensing analysis has a $b_1\sigma_8^2$ degeneracy, which is effectively broken when combined with the galaxy 2PCF.

- We have performed many tests to check the robustness of our results against non-linear effects, which are expected to be relevant on the scales probed here and are the reason for the conservative cut at $s_{min} = 15 h^{-1}$ Mpc. Decreasing s_{min} reduces parameter errors from the 2PCF only analysis but also picks up a negative value for γ , in mild tension (given the considerable uncertainty) with the joint 2PCF-3PCF analysis and previous VIPERS analyses. On the contrary, reducing s_{min} does not have a significant impact on the 3PCF and the joint analyses. In Table 4 we list the best fit values of σ_8 , f , b_1 and γ obtained for different choices of s_{min} . Errors increase when s_{min} increases, as a result of the reduction of the number of pairs/triplets and scales included in the analysis. In particular, with $s_{min} = 20 h^{-1}$ Mpc no significant constraints can be set on γ . A detailed analysis of the sensitivity of our results to the choice of s_{min} is presented in Appendix C.

Our work confirms the importance of clustering analyses beyond 2-point statistics. Here, we were able to break parameter degeneracies using a relatively modest number of objects (23352 and 13046 for the G1 and G2 samples, respectively). In this respect, this work represents a successful pilot study in the preparation for the next generation spectroscopic surveys, such as the DESI project, the *Euclid* (Laureijs et al. 2011) and the *Roman* (Akeson et al. 2019) space telescope missions. These surveys will be able to perform clustering analyses on scales much larger than those considered

Table 4. Best-fit values of the parameters obtained in the joint analysis of 2PCF and 3PCF, using different values of s_{min} . The values of s_{min} are in h^{-1} Mpc. All the constraints are compatible, within 1σ .

Sample	s_{min}	$\sigma_8(z)$	f	b_1	γ
G1	10	0.4 ± 0.1	$1.0^{+0.7}_{-0.5}$	$1.8^{+0.4}_{-0.3}$	-0.1 ± 0.6
	15	0.5 ± 0.1	$0.6^{+0.6}_{-0.4}$	1.6 ± 0.4	$-0.1^{+0.9}_{-1.3}$
	20	$0.4^{+0.3}_{-0.2}$	$1.1^{+1.6}_{-1.0}$	$0.5^{+0.7}_{-0.4}$	unconstrained
G2	10	0.3 ± 0.1	$1.4^{+1.2}_{-0.8}$	$2.0^{+1.0}_{-0.6}$	$-1.1^{+1.4}_{-2.2}$
	15	0.4 ± 0.1	1.0 ± 1.0	$1.9^{+0.8}_{-0.5}$	$0.5^{+1.3}_{-1.2}$
	20	$0.2^{+0.2}_{-0.1}$	$0.9^{+1.4}_{-0.8}$	$1.8^{+1.9}_{-0.9}$	$-0.2^{+1.5}_{-3.9}$

here. However, small scales will still encode an even larger amount of information. Its extraction will require measuring higher-order statistics and comparing results to non-linear models, as we have done in this work. In this respect, one of the main lessons learned from our analysis is the need to develop a full 1-loop model for the 3PCF, matching the 2PCF one, which we plan to present in future work.

The availability of such a model, along with that of a new generation of efficient 3PCF estimators (Slepian & Eisenstein 2015, 2016), would make higher-order clustering analyses in configuration space more palatable and a serious contender to more traditional Fourier-space methods. Bispectrum analyses enjoy the availability of fast estimators and non-linear models. However, they suffer from mode coupling induced by complex survey geometries, which is difficult to account for. Comparing the performances of joint 2-point and 3-point clustering analyses in configuration and Fourier space for next-generation spectroscopic surveys is another open issue, which we plan to investigate in the future.

Finally, in this analysis, we were able to break parameter degeneracies using higher-order statistics. Alternatively, it can be broken by combining 2-point clustering and gravitational lensing, as in de la Torre et al. (2017). Both approaches have advantages and disadvantages. The 2- and 3-point clustering analysis requires a single (spectroscopic) dataset to be performed. However, it is less efficient in removing parameters' degeneracy. The clustering-lensing

analysis is more effective in breaking degeneracy but needs both a photometric and a spectroscopic survey to be performed. How to best combine these two types of analyses is another interesting issue that deserves a dedicated future study.

DATA AVAILABILITY

The VIPERS PDR2 data, as well as the mock samples used here are publicly available from the VIPERS web site (<http://vipers.inaf.it>). The clustering measurements and covariance matrices from this paper are available from the authors, upon request.

ACKNOWLEDGEMENTS

AV and EB thank Emiliano Sefusatti, Alexander Eggemeier, Elena Sarpa, Massimo Guidi for useful discussions. This paper uses data from the VIMOS Public Extragalactic Redshift Survey (VIPERS). VIPERS has been performed using the ESO Very Large Telescope, under the “Large Programme” 182.A-0886. The participating institutions and funding agencies are listed at <http://vipers.inaf.it>. AV, EB, LG and LM are supported by ASI/INAF agreement n. 2018-23-HH.0 “Scientific activity for Euclid mission, Phase D” and INFN project “InDark”. EB and LG are further supported by MIUR/PRIN 2017 “From Darklight to Dark Matter: understanding the galaxy-matter connection to measure the Universe”. EB is also supported by ASI/INAF agreement n. 2017-14-H.O “Unveiling Dark Matter and Missing Baryons in the high-energy sky”. MM acknowledges the grants ASI n.I/023/12/0, ASI n.2018-23-HH.0, and support from MIUR, PRIN 2017 (grant 20179ZF5KS). This research was supported by the Munich Institute for Astro- and Particle Physics (MIAPP) which is funded by the Deutsche Forschungsgemeinschaft (DFG, German Research Foundation) under Germany’s Excellence Strategy- EXC - 2094 - 390783311. LM also acknowledge the support from the grant PRIN-MIUR 2017 WSCC32.

REFERENCES

Adams C., Blake C., 2017, *MNRAS*, **471**, 839
Akeson R., et al., 2019, arXiv e-prints, p. [arXiv:1902.05569](https://arxiv.org/abs/1902.05569)
Alam S., et al., 2021, *Phys. Rev. D*, **103**, 083533
Alcock C., Paczynski B., 1979, *Nature*, **281**, 358
Baldauf T., Seljak U., Desjacques V., McDonald P., 2012, *Phys. Rev. D*, **86**, 083540
Bel J., Pezzotta A., Carbone C., Sefusatti E., Guzzo L., 2019, *A&A*, **622**, A109
Bernardeau F., Colombi S., Gaztañaga E., Scoccimarro R., 2002, *Phys. Rep.*, **367**, 1
Beutler F., et al., 2012, *MNRAS*, **423**, 3430
Beutler F., et al., 2014, *MNRAS*, **443**, 1065
Blake C., et al., 2012, *MNRAS*, **425**, 405
Blake C., et al., 2013, *MNRAS*, **436**, 3089
Cappi A., et al., 2015, *A&A*, **579**, A70
Chan K. C., Scoccimarro R., Sheth R. K., 2012, *Phys. Rev. D*, **85**, 083509
Cole S., et al., 2005, *MNRAS*, **362**, 505
DESI Collaboration et al., 2016a, arXiv e-prints, p. [arXiv:1611.00036](https://arxiv.org/abs/1611.00036)
DESI Collaboration et al., 2016b, arXiv e-prints, p. [arXiv:1611.00037](https://arxiv.org/abs/1611.00037)
Davidzon I., et al., 2016, *A&A*, **586**, A23
Davis M., Nusser A., Masters K. L., Springob C., Huchra J. P., Lemson G., 2011, *MNRAS*, **413**, 2906
Di Porto C., et al., 2016, *A&A*, **594**, A62
Eisenstein D. J., et al., 2005, *ApJ*, **633**, 560
Fry J. N., 1994, *Phys. Rev. Lett.*, **73**, 215

Garilli B., et al., 2014, *A&A*, **562**, A23
Gaztañaga E., Cabré A., Castander F., Crocce M., Fosalba P., 2009, *MNRAS*, **399**, 801
Gil-Marín H., Wagner C., Noreña J., Verde L., Percival W., 2014, *J. Cosmology Astropart. Phys.*, **2014**, 029
Gil-Marín H., Noreña J., Verde L., Percival W. J., Wagner C., Manera M., Schneider D. P., 2015, *MNRAS*, **451**, 539
Gil-Marín H., Percival W. J., Verde L., Brownstein J. R., Chuang C.-H., Kitaura F.-S., Rodríguez-Torres S. A., Olmstead M. D., 2017, *MNRAS*, **465**, 1757
Granett B. R., Favole G., Montero-Dorta A. D., Branchini E., Guzzo L., de la Torre S., 2019, *MNRAS*, **489**, 653
Groth E. J., Peebles P. J. E., 1977, *ApJ*, **217**, 385
Guo H., Li C., Jing Y. P., Börner G., 2014, *ApJ*, **780**, 139
Guo H., et al., 2015, *MNRAS*, **449**, L95
Guzzo L., et al., 2008, *Nature*, **451**, 541
Guzzo L., et al., 2014, *A&A*, **566**, A108
Hamilton A. J. S., 2000, *MNRAS*, **312**, 257
Hartlap J., Simon P., Schneider P., 2007, *A&A*, **464**, 399
Hawken A. J., et al., 2017, *A&A*, **607**, A54
Hoffmann K., Gaztañaga E., Scoccimarro R., Crocce M., 2018, *MNRAS*, **476**, 814
Hui L., Gaztañaga E., 1999, *ApJ*, **519**, 622
Huterer D., Linder E. V., 2007, *Phys. Rev. D*, **75**, 023519
Huterer D., Shafer D. L., Scolnic D. M., Schmidt F., 2017, *J. Cosmology Astropart. Phys.*, **2017**, 015
Jing Y. P., Börner G., 2004, *ApJ*, **607**, 140
Jullo E., et al., 2019, *A&A*, **627**, A137
Kaiser N., 1987, *MNRAS*, **227**, 1
Kayo I., et al., 2004, *PASJ*, **56**, 415
Kazin E. A., et al., 2013, *MNRAS*, **435**, 64
Klypin A., Yepes G., Gottlöber S., Prada F., Heß S., 2016, *MNRAS*, **457**, 4340
Kulkarni G. V., Nichol R. C., Sheth R. K., Seo H.-J., Eisenstein D. J., Gray A., 2007, *MNRAS*, **378**, 1196
Landy S. D., Szalay A. S., 1993, *ApJ*, **412**, 64
Laureijs R., et al., 2011, arXiv e-prints, p. [arXiv:1110.3193](https://arxiv.org/abs/1110.3193)
Lesgourgues J., 2011, arXiv e-prints, p. [arXiv:1104.2932](https://arxiv.org/abs/1104.2932)
Lewis A., Challinor A., Lasenby A., 2000, *ApJ*, **538**, 473
Maartens R., Abdalla F. B., Jarvis M., Santos M. G., 2015, arXiv e-prints, p. [arXiv:1501.04076](https://arxiv.org/abs/1501.04076)
Marín F., 2011, *ApJ*, **737**, 97
Marín F. A., et al., 2013, *MNRAS*, **432**, 2654
Marulli F., Bianchi D., Branchini E., Guzzo L., Moscardini L., Angulo R. E., 2012, *MNRAS*, **426**, 2566
Marulli F., et al., 2013, *A&A*, **557**, A17
Marulli F., Veropalumbo A., Moresco M., 2016, *Astronomy and Computing*, **14**, 35
Marulli F., Veropalumbo A., García-Farieta J. E., Moresco M., Moscardini L., Cimatti A., 2020, arXiv e-prints, p. [arXiv:2010.11206](https://arxiv.org/abs/2010.11206)
Matarrese S., Verde L., Heavens A. F., 1997, *MNRAS*, **290**, 651
McBride C. K., Connolly A. J., Gardner J. P., Scranton R., Newman J. A., Scoccimarro R., Zehavi I., Schneider D. P., 2011a, *ApJ*, **726**, 13
McBride C. K., Connolly A. J., Gardner J. P., Scranton R., Scoccimarro R., Berlind A. A., Marín F., Schneider D. P., 2011b, *ApJ*, **739**, 85
McDonald P., Roy A., 2009, *J. Cosmology Astropart. Phys.*, **2009**, 020
Mohammad F. G., et al., 2018, *A&A*, **610**, A59
Moresco M., Marulli F., Baldi M., Moscardini L., Cimatti A., 2014, *MNRAS*, **443**, 2874
Moresco M., et al., 2017, *A&A*, **604**, A133
Moresco M., Veropalumbo A., Marulli F., Moscardini L., Cimatti A., 2020, arXiv e-prints, p. [arXiv:2011.04665](https://arxiv.org/abs/2011.04665)
Nichol R. C., et al., 2006, *MNRAS*, **368**, 1507
Okumura T., et al., 2016, *PASJ*, **68**, 38
Peacock J. A., et al., 2001, *Nature*, **410**, 169
Pearson D. W., Samushia L., 2019, *MNRAS*, **486**, L105
Percival W. J., et al., 2014, *MNRAS*, **439**, 2531
Pezzotta A., et al., 2017, *A&A*, **604**, A33

- Planck Collaboration et al., 2016, *A&A*, 594, A13
 Planck Collaboration et al., 2020, *A&A*, 641, A6
 Rota S., et al., 2017, *A&A*, 601, A144
 Saito S., Baldauf T., Vlah Z., Seljak U., Okumura T., McDonald P., 2014, *Phys. Rev. D*, 90, 123522
 Scoccimarro R., 2004, *Phys. Rev. D*, 70, 083007
 Scoccimarro R., Zaldarriaga M., Hui L., 1999, *ApJ*, 527, 1
 Scodeggio M., et al., 2018, *A&A*, 609, A84
 Sefusatti E., Crocce M., Pueblas S., Scoccimarro R., 2006, *Phys. Rev. D*, 74, 023522
 Sellentin E., Heavens A. F., 2016, *MNRAS*, 456, L132
 Sereno M., Veropalumbo A., Marulli F., Covone G., Moscardini L., Cimatti A., 2015, *MNRAS*, 449, 4147
 Shi F., et al., 2018, *ApJ*, 861, 137
 Singh S., Alam S., Mandelbaum R., Seljak U., Rodriguez-Torres S., Ho S., 2019, *MNRAS*, 482, 785
 Slepian Z., Eisenstein D. J., 2015, *MNRAS*, 454, 4142
 Slepian Z., Eisenstein D. J., 2016, *MNRAS*, 455, L31
 Slepian Z., Eisenstein D. J., 2017, *MNRAS*, 469, 2059
 Slepian Z., Eisenstein D. J., 2018, *MNRAS*, 478, 1468
 Slepian Z., et al., 2017a, *MNRAS*, 468, 1070
 Slepian Z., et al., 2017b, *MNRAS*, 469, 1738
 Sugiyama N. S., Saito S., Beutler F., Seo H.-J., 2020, *MNRAS*, 497, 1684
 Szapudi I., 2004, *ApJ*, 605, L89
 Szapudi I., Szalay A. S., 1998, *ApJ*, 494, L41
 Takahashi R., Sato M., Nishimichi T., Taruya A., Oguri M., 2012, *ApJ*, 761, 152
 Taruya A., Nishimichi T., Saito S., 2010, *Phys. Rev. D*, 82, 063522
 Wang L., Steinhardt P. J., 1998, *ApJ*, 508, 483
 Yankelevich V., Porciani C., 2019, *MNRAS*, 483, 2078
 de la Torre S., et al., 2013, *A&A*, 557, A54
 de la Torre S., et al., 2017, *A&A*, 608, A44
 eBOSS Collaboration et al., 2020, arXiv e-prints, p. arXiv:2007.08991

APPENDIX A: 3PCF ESTIMATOR BINNING

The algorithm of Slepian & Eisenstein (2015) used in this work estimates the multipole coefficients of the 3PCF Legendre expansion in radial bins $\Delta_{r_{12}}$ and $\Delta_{r_{13}}$, $\zeta_l(\Delta_{r_{12}}, \Delta_{r_{13}})$. To obtain an unbiased estimate of $\zeta(\Delta_{r_{12}}, \Delta_{r_{13}}, \Delta_\mu)$ in bins Δ_μ , one needs to use bin-averaged Legendre polynomials $\bar{\mathcal{P}}_l(\Delta_\mu)$, i.e.

$$\zeta(\Delta_{r_{12}}, \Delta_{r_{13}}, \Delta_\mu) = \sum_{l=0}^{l_{max}} \zeta_l(\Delta_{r_{12}}, \Delta_{r_{13}}) \bar{\mathcal{P}}_l(\Delta_\mu), \quad (\text{A1})$$

where

$$\bar{\mathcal{P}}_l(\Delta_\mu) \equiv \bar{\mathcal{P}}_l(\mu_{min} \leq \mu \leq \mu_{max}) = \frac{1}{\Delta_\mu} \left[\frac{\mathcal{P}_{l+1}(\mu) - \mathcal{P}_{l-1}(\mu)}{2l+1} \right]_{\mu_{min}}^{\mu_{max}}, \quad (\text{A2})$$

in the bin $\Delta_\mu = [\mu_{min}, \mu_{max}]$; when $l = 0$, $\bar{\mathcal{P}}_{l=0}(\Delta_\mu) = 1$.

In this work, we express the 3PCF as a function of r_{23} , rather than μ , with the two quantities related through the relation

$$\mu = \frac{r_{12}^2 + r_{13}^2 - r_{23}^2}{2r_{12}r_{13}}, \quad (\text{A3})$$

so that, given r_{12} and r_{13} , the cosine angle μ varies in the range $[0, 1]$, whereas r_{23} varies between $|r_{12} - r_{13}|$ and $|r_{12} + r_{13}|$. One can show that in this case the binned Legendre polynomials are of the form

$$\bar{\mathcal{P}}_l(\Delta_{r_{12}}, \Delta_{r_{13}}, \Delta_{r_{23}}) = \frac{32\pi}{V_{12}V_{13}} \int k^2 I_l(k; \Delta_{r_{12}}) I_l(k; \Delta_{r_{13}}) I_0(k; \Delta_{r_{23}}) dk, \quad (\text{A4})$$

where V_{12} and V_{13} represent the volume of the spherical shells of width $\Delta_{r_{12}}, \Delta_{r_{13}}$ respectively, and

$$I_l(k; \Delta_r) = \int_{r_{min}}^{r_{max}} r^2 j_l(kr) dr, \quad (\text{A5})$$

where $j_l(kr)$ are spherical Bessel functions.

APPENDIX B: EXPLICIT EXPRESSIONS FOR THE 3PCF MODEL

The explicit expression of the A_l terms that appear in Eq. (25) is

$$\begin{aligned} A_0 &= b_1^3 \left\{ \frac{34}{21} \left[1 + \frac{4}{3}\beta + \frac{1154}{1275}\beta^2 + \frac{936}{2975}\beta^3 + \frac{21}{425}\beta^4 \right] \right. \\ &\quad \left. + \gamma \left[1 + \frac{2}{3}\beta + \frac{1}{9}\beta^2 \right] + \frac{16}{675}\beta^2 \gamma' \right\}, \\ A_1 &= -b_1^3 \left[1 + \frac{4}{3}\beta + \frac{82}{75}\beta^2 + \frac{12}{25}\beta^3 + \frac{3}{35}\beta^4 \right], \\ A_2 &= b_1^3 \left\{ \frac{8}{21} \left[1 + \frac{4}{3}\beta + \frac{52}{21}\beta^2 + \frac{81}{49}\beta^3 + \frac{12}{35}\beta^4 \right] \right. \\ &\quad \left. + \frac{32\gamma}{945}\beta^2 + \frac{5}{2} \left(\frac{8}{15} + \frac{16\beta}{45} + \frac{344\beta^2}{4725} \right) \gamma' \right\}, \\ A_3 &= -b_1^3 \left[\frac{8}{75}\beta^2 + \frac{16}{175}\beta^3 + \frac{8}{315}\beta^4 \right], \\ A_4 &= b_1^3 \left[-\frac{32}{3675}\beta^2 + \frac{32}{8575}\beta^3 + \frac{128}{11025} \right]. \end{aligned} \quad (\text{B1})$$

In the same equation, the f_l terms are:

$$f_l(r_{12}, r_{13}, r_{23}) = \begin{cases} \xi^{[l]}(r_{12}) \xi^{[l]}(r_{13}) \mathcal{L}_l(\mu_{23}) + \text{cyc.} & \text{if } l \text{ is even} \\ \left[\xi^{[l+]}(r_{12}) \xi^{[l-]}(r_{13}) + \right. \\ \left. \xi^{[l+]}(r_{13}) \xi^{[l-]}(r_{12}) \right] \mathcal{L}_l(\mu_{23}) + \text{cyc.} & \text{if } l \text{ is odd,} \end{cases} \quad (\text{B2})$$

where

$$\xi_i^{[l]} = \int \frac{k^2 dk}{2\pi^2} 2\pi^2 P_{lin}(k) j_l(kr_i) \quad (\text{B3})$$

$$\xi_i^{[l\pm]} = \int \frac{k^2 dk}{2\pi^2} k^{\pm 1} P_{lin}(k) j_l(kr_i).$$

and $P_{lin}(k)$ is the linear matter power spectrum.

APPENDIX C: SENSITIVITY TO NONLINEAR EFFECTS

Since our clustering analysis includes scales smaller than $40h^{-1}$ Mpc, nonlinear effects in both dynamics and galaxy bias cannot be neglected. To minimise the impact of potential systematic errors derived from an incorrect model of these effects, we have adopted a conservative approach and excluded scales below $15h^{-1}$ Mpc from the analysis. These are scales, however, where a significant amount of cosmological information is stored. In this Appendix, we use the realistic mock VIPERS catalogues to perform several tests to assess the sensitivity of our results to the choice of this minimum scale, s_{min} . We are confident that these tests provide useful indications for the real data analysis since, as we have discussed in Sect. 3, the 2- and 3-point correlation functions measured

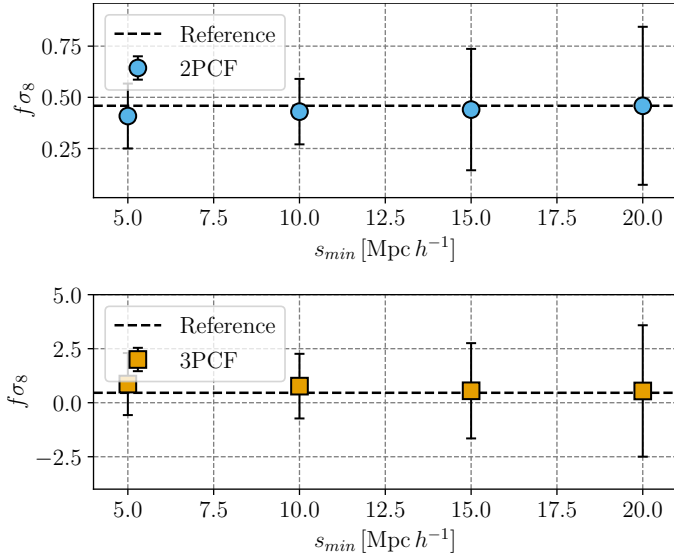


Figure C1. Average estimates over the 153 mock samples of $f\sigma_8$ using the 2PCF (top, filled points) and the 3PCF (bottom, filled squares), as a function of the minimum scale included in the analysis, s_{min} . The black dashed line in both cases gives the reference value, corresponding to the cosmology of the simulated mocks, while error bars are given by the scatter among the mocks. Note how the error bars for the 3PCF estimates are ~ 10 times larger than those from the 2PCF, due to the fact that for the latter only the monopole (i.e. the isotropic information), has been considered.

in the mocks agree well with those measured on the real data on all scales considered here.

Let us first consider the parameter combination $f\sigma_8$, as obtained from the 2PCF and the 3PCF. We show here the results from the G2 sample only, since they are representative of the generality of the results. In Fig. C1 we show the average and *rms* scatter over the 153 mocks of the value of $f\sigma_8$ estimated using the 2PCF and the 3PCF (top and bottom panels, respectively), as a function of s_{min} . The results show that including scales as small as $5 h^{-1}$ Mpc significantly reduces the statistical error without compromising the accuracy. This conclusion is true for both the 2PCF and the 3PCF cases, indicating that the models we have used are adequate for measuring this parameter combination.

Things are different when one tries to break the parameter degeneracy through the joint 2PCF and 3PCF analysis, as shown in Fig. C2. In the two panels, the average estimates of σ_8 (top) and f (bottom) are plotted as a function of s_{min} . Note how the size of the error bars decreases, when smaller scales are progressively included in the analysis. For $s_{min} = 5 h^{-1}$ Mpc they are significantly smaller than in our baseline case ($s_{min} = 15 h^{-1}$ Mpc). However, while random errors decrease, systematic errors increase: the value of σ_8 is systematically underestimated in general (although at the 1σ level only) and, to compensate, the measured growth rate is larger than the true one. These results justify our conservative choice to set $s_{min} = 15 h^{-1}$ Mpc and indicate that a better modelling is required to push a joint 2PCF and 3PCF analysis to smaller scales.

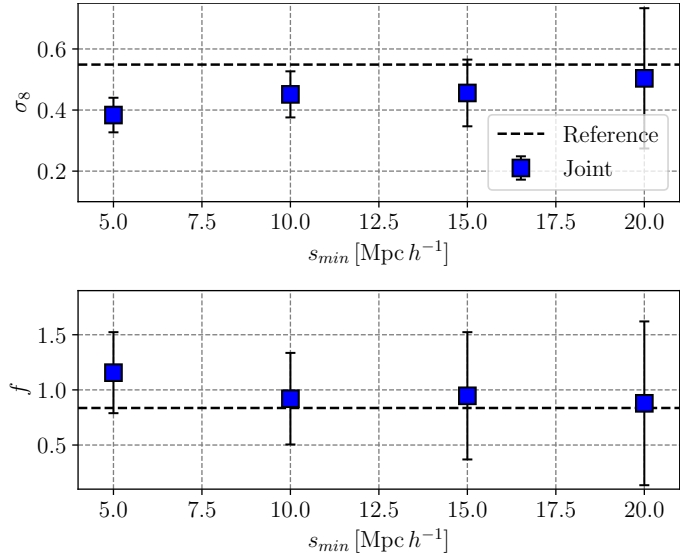


Figure C2. Average estimates of $f(z)$ and $\sigma_8(z)$ from the joint 2PCF-3PCF analysis of the 153 mocks (filled blue squares), compared to the reference cosmology (black dashed line). As usual, error bars are the standard deviation over the mocks. While the estimates of $f(z)$ are robust, recovering the input value of the mocks, there is a small bias for σ_8 (still within 1σ at the reference $s_{min} = 15 h^{-1}$ Mpc).